Supercritical Water Radiolysis Chemistry
Supercritical Water Corrosion

D.M. Bartels, University of Notre Dame
M. Anderson, University of Wisconsin
P. Wilson, University of Wisconsin
T. Allen, University of Wisconsin
K. Sridharan, University of Wisconsin

Executive Summary

Research Objectives

The direct measurement of the chemistry in reactor cores is extremely difficult. The extreme conditions of high temperature, pressure, and radiation fields, are not compatible with normal chemical instrumentation. There are also problems of access to fuel channels in the reactor core. For these reasons, all reaction vendors and many operators have extensively used theoretical calculations and chemical models to model the detailed radiation chemistry of the water in the core and the consequences for materials. The results of these model calculations can be no more accurate than the fundamental information fed into them, and serious discrepancies remain between model calculations and reactor experiments [1,2,3]. For proposed supercritical water cooled reactors, there is barely any information available to begin construction of a radiolysis model for the anticipated pressure (250bar) and temperatures (up to 500^{o}C). The objective of this work is to generate the necessary radiation chemistry data (yields and reaction rates) needed to model chemistry in a supercritical water cooled reactor. Beta/gamma yields and reaction rates are measured using electron accelerators at Notre Dame University. Yields from neutron radiolysis are being measured at the University of Wisconsin Reactor Facility. The initial goal is to at least estimate corrosion potentials likely to prevail in the core of such a reactor. This will guide design and feasibility studies for the primary heat transport system. At both facilities, an evaluation is being made of the use of added hydrogen to suppress supercritical water.

Research Accomplishments

Beta/gamma yields. A large amount of data has been collected and tabulated for the yields of $(e^-)_{aq}$, H atom, and H_2 molecule [3]. Data was collected along a 250bar isobar up to 400^{o}C, and also as a function of water density (pressure) at supercritical temperatures 380^{o}C and 400^{o}C. Accurate measurements at higher temperature become harder due to H_2 generated by thermal corrosion reactions. These data allow us to define a yield or G-value for reducing equivalents, G(red), which by mass balance is also equal to the yield of oxidizing equivalents G(ox) and to the yield of water dissociation $G(-H_2O)$. Using just these data it should be possible to estimate the order of magnitude of peroxide and oxygen produced by radiolysis, and estimate corrosion potentials.

Neutron yields. A large amount of data has been collected for yields of $(e^-)_{aq}$, H atom, and H_2 molecule in two different mixed neutron/gamma radiation fields as a function of

temperature up to 420°C. Numerous calibrations have been carried out along with a large number of simulations allow us to separate the neutron and gamma yield components.

Reaction Rates. Measurement of second order reaction rates for the primary radicals $(e^-)_{aq}$, H atom, and OH is extremely difficult because of the need to determine absolute concentrations of the transient species [4]. We have succeeded in measuring three of the six recombination reactions up to 350°C. Another reaction is in process of being measured, while a fifth can be reliably estimated. The behavior up to 350°C gives us a good idea of which reactions may be most important in supercritical water, but a full accurate model of supercritical water recombination chemistry is still some years away.

Critical Hydrogen Concentration. The question is whether "hydrogen water chemistry" will still work to suppress radiolysis and stress corrosion cracking at supercritical temperatures? Experiments looking at the suppression of oxygen production suggest it will work [5], but the concentration of added H_2 must be higher for supercritical water, because the absolute density of the H_2 in the core decreases right along with the absolute density of the water. In these experiments we have also found a strange production of additional hydrogen from radiolysis that we are still investigating.

Corrosion. Corrosion studies have elucidated the general response of alloy classes to supercritical water exposure. Ferritic-martensitic steels have a stable weigh gain to 1000 hours but a method to control the very heavy oxidation must be found before these steels can be used for thin-walled components. Austenitic stainless steels have a smaller weigh gain but oxides are not always stable. Nickel-base alloys have very little weight gain and from a corrosion standpoint are the best candidates for SCW use. Unfortunately, their radiation response may prevent limit their performance. Surface modification and grain boundary engineering techniques are being pursued to eliminate the heavy oxidation problem in ferritic-martensitic steels and the spallation problem in austenitic steels. Both techniques have shown promise.

1. Beta/Gamma Radiolysis Yields

Perhaps the most important quantity to know when starting to model the radiation chemistry is the escape yields from tracks and spurs, which is quantified in terms of the G-value: number of molecules or radicals produced per unit radiation energy deposited. Traditionally the units were given in terms of molecules per 100eV of energy [4]. More recently proper SI units of moles/J are used [6]. The numbers are very similar, but the SI unit is 10^7 times smaller. To provide a scale, it takes 5.2 eV to dissociate a water O-H bond, and 12.6eV to ionize in vacuum. However because of solvation stabilization, it requires only 5.8eV to produce the fully solvated $(e^-)_{aq}$, OH radical, and $(H_3O^+)_{aq}$. So the absolute largest G value that is possible in pure water radiolysis is 19.2 H or OH per 100eV of energy. Or for $(e^-)_{aq}$, it would be 17.2 per 100eV. At room temperature, the escape yield of $(e^-)_{aq}$ and of OH is around 2.7 per 100eV. Of course, eventually all of these reactive radicals will recombine, and their ultimate yield is zero. We are actually more concerned with the yield of the H_2 and H_2O_2 product of recombination. The latter product is impossible to measure quantitatively because of its catalytic decomposition on surfaces, and so we attempt to estimate its transient concentration by modeling, which requires the yields and rate constants of all of the species in the system. We describe below new measurements of the products $(e^-)_{aq}$, H atom, and H_2 in supercritical water conditions.

1.1 Experimental

The β-radiolysis experiments were performed at the Notre Dame Radiation Laboratory using a custom made supercritical water cell (SCW) and 2.5 MeV electrons from a Van de Graaff (VdG) accelerator [7]. The apparatus consisted of sample reservoirs and pumps, a high

pressure/temperature irradiation flowtube, and ambient pressure/temperature analysis setup with directly coupled mass spectrometer (Figure 1.1A).

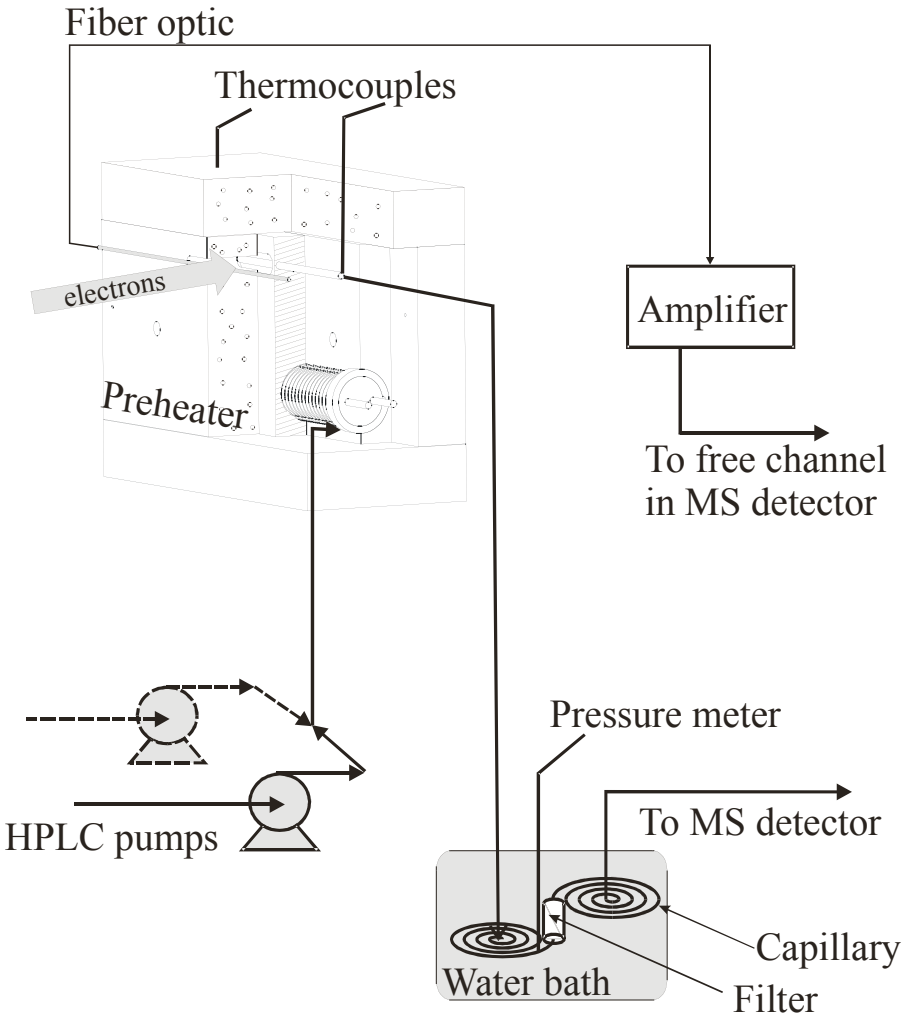

Figure 1.1A. Schematic of the apparatus for beta radiolysis yield measurements.

The high temperature/pressure flow cell consisted of two partially separated sections. In the lower section the solutions were pumped through hastelloy C276 1/16 inch tubing that was wrapped around a cylindrical electric preheater. Then after preheating, solution was introduced to an irradiation zone made from 1/8 inch titanium tubing (0.06 mL total volume) in the upper section. Behind the irradiation zone a second cartridge heater was placed to maintain the temperature and compensate for the electron beam heating. The temperature of solution before

and after the irradiation zone was monitored with a pair of thermocouples. The entire assembly was enclosed in a stainless steel block (with a window cut for easier electron penetration through the irradiation volume) and placed in an insulating box. A fiber-optic was placed in a slit in the insulation in front of the irradiated tubing to monitor the dose by means of generated Cerenkov light and fluorescence. The optical signal was detected by a silicon photodiode and after amplification was monitored in one of the spare A/D channels in the mass spectrometer (MS) along with the molecular ion signals.

To analyze dissolved gases, precisely 12.0 mL (2 minutes collecting time at flow 6 mL/min) of irradiated solution was collected in the sparging vessel, and then bubbled with UHP argon. The argon stripped out any gaseous products from the irradiated solutions and carried them through the water trap (0.25 inch OD, 3 meter long coiled column packed with 4A Molecular Sieves) towards the inlet of the mass spectrometer capillary. The capillary, made from 3 cm long and 25 μm ID fused silica uncoated tubing, was placed in the side arm of a T-connection to allow sampling from the center of the main gas stream. Molecular ion signals of the gaseous products were monitored as a function of time with a Balzers/Pfeiffer QMS 200 quadrupole mass spectrometer.

Radiolysis experiments were performed using a DC electron beam to produce absorbed doses in the range 100-700 Gy. The maximum dose was limited by the concentration of solvated electron generated during the experiment. Final concentrations larger than 2.5×10^{-4} m would imply 10 % conversion of the available N_2O. This concentration corresponds roughly to 1000 Gy and was never exceeded during the course of the experiments. Solutions were in the irradiation zone for 0.6 second, which for the applied doses corresponds to a dose rate of 300 – 1200 Gy s^{-1}.

1.2 Results

During water radiolysis a number of transient and stable products are produced. The initial reaction can be summarized with the equation:

$$H_2O \xrightarrow{irr} e^-_{aq}, {}^{\bullet}OH, H^{\bullet}, H^+, OH^-, H_2O_2, H_2$$

It should be understood that the "yields" of H^+, e^-_{aq}, $^{\bullet}OH$, and $H^{\bullet}$ in particular are functions of time because of fast recombination. Scavenged yields of these species, typically for the first order scavenging rate or "scavenging power "(i.e. rate constant times scavenger concentration) of 1.0×10^7 s^{-1}, are very well established at room temperature[9]. Nitrous oxide (N_2O) is well known as a useful and very efficient hydrated electron scavenger[10]. Its reduction in reaction (1) leads to the stable gas nitrogen.

$$e^-_{aq} + N_2O \xrightarrow{H_2O} {}^{\bullet}OH^- + OH^- + N_2 \qquad (1)$$

However, N_2O can also react with H atoms giving the same product in reaction (2)[12].

$$H^{\bullet} + N_2O \rightarrow {}^{\bullet}OH + N_2 \qquad (2)$$

The low value of rate coefficient for this reaction at room temperature does not necessarily imply the same at higher temperatures. Among many possible scavengers phenol molecules are known to react rapidly with both $^{\bullet}OH$ and $H^{\bullet}$ atoms but quite moderately with electrons[10,13]. The N_2 and H_2 radiolysis yield in the N_2O/phenol system should therefore correspond to the solvated electron and molecular hydrogen formed in spurs, respectively.

The experiments performed with the phenol/N_2O solution give us solid information about molecular hydrogen as well as solvated electron radiation yields in a wide range of temperatures and densities. Reactions of H and OH with ethanol-d5 are similar to normal ethanol, but abstraction of deuterium leads to a different gas product as indicated in reaction (3):

$$H^{\bullet} + C_2D_5OH \rightarrow HD + (C_2D_4OH)^{\bullet} \quad (3)$$

$$^{\bullet}OH + C_2D_5OH \rightarrow HDO + (C_2D_4OH)^{\bullet} \quad (4)$$

In this system, HD produced instead of H_2 gives an easily detectable and specific ion mass signal corresponding to the hydrogen atom. The pairing of this deuterated alcohol in solution with N_2O then should allow simultaneous measurement of yields for molecular H_2, H atom (as HD), and hydrated electron (as N_2). However we discovered that above 200°C the N_2 yields were too high in the ethanol-d5 system to correspond to just hydrated electron scavenging. The alcohol radicals formed in (3) and (4) are able to reduce N_2O as well and give additional N_2 signal from a radical chain reaction. For this reason we use only the N_2 yields with phenol as the H and OH scavenger.

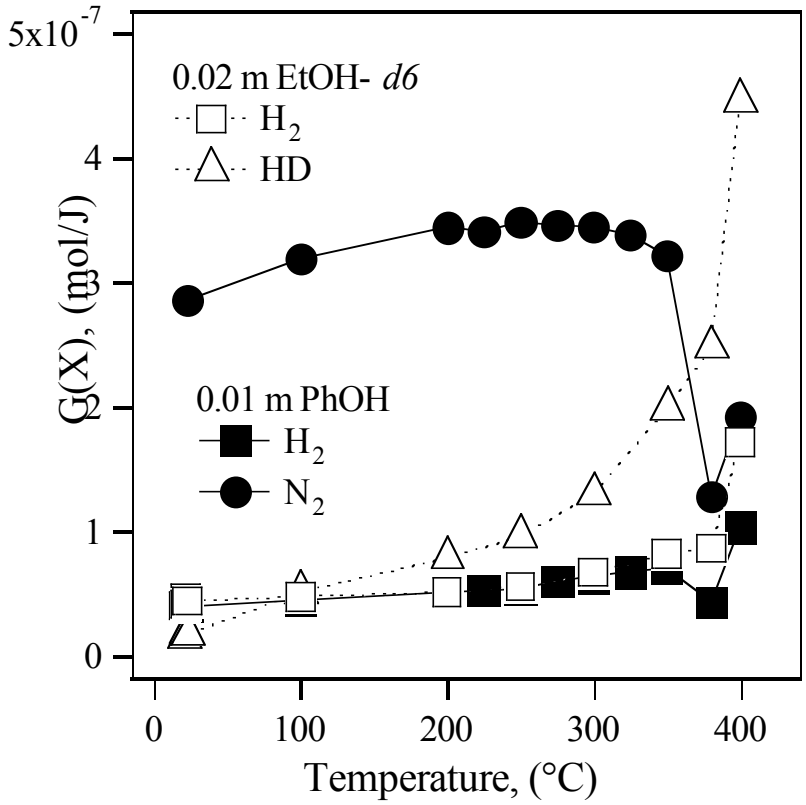

Figure 1.2A. Beta radiolysis G-values as a function of temperature in water at 250 bar.

Table 1.2A. G values at 250 bar pressure

Temperature (°C)	Density (kg dm^{-3})	G(X) $\times 10^{-7}$ (mol J^{-1})				
		in 0.01m PhOH		in 0.02m EtOH-d6		
		H_2	N_2	H_2	HD	N_2
22	1.0000	0.39	2.86	0.44	0.18	2.83
100	0.9696	0.45	3.19	0.47	0.51	3.23
200	0.8813	0.51	3.44	0.51	0.78	3.55
225	0.8527	0.51	3.41	–	–	–
250	0.8209	0.54	3.49	0.56	0.95	3.65
275	0.7848	0.60	3.46	–	–-	–-
300	0.7430	0.63	3.45	0.67	1.30	4.19
325	0.6926	0.67	3.38	–	–-	–-
350	0.6271	0.71	3.22	0.82	1.98	4.02
380	0.4508	0.43	1.28	0.86	2.48	1.23
400	0.1665	1.03	1.92	1.72	4.46	1.93

In figure 1.2A we plot the $(e^-)_{aq}$ yield (as N_2) and the H_2 yield from the phenol/N_2O system along with the H atom yield (as HD) and the H_2 yield from ethanol-d5/N_2O. The $(e^-)_{aq}$ yield increases up to about 250°C, then begins a decline and drops dramatically to a minimum at 380°C near the critical temperature. The H atom yield rises continuously into the critical regime. In comparing values of H_2 listed for both ethanol-d5 and phenol we see a very good agreement up to 300 °C. At temperatures 350 °C and above we found somewhat higher yields of H_2 in ethanol-d6. This was a surprise, but was explained in terms of the abstraction of the hydroxyl proton in C_2D_5OH, to give H_2 product. Reaction

$$H^{\bullet} + C_2D_5OH \rightarrow H_2 + (C_2D_5O)^{\bullet} \qquad (5)$$

(5) is negligible at low temperature, but becomes comparable to the rate of abstraction of D from the carbon atoms at 400°C

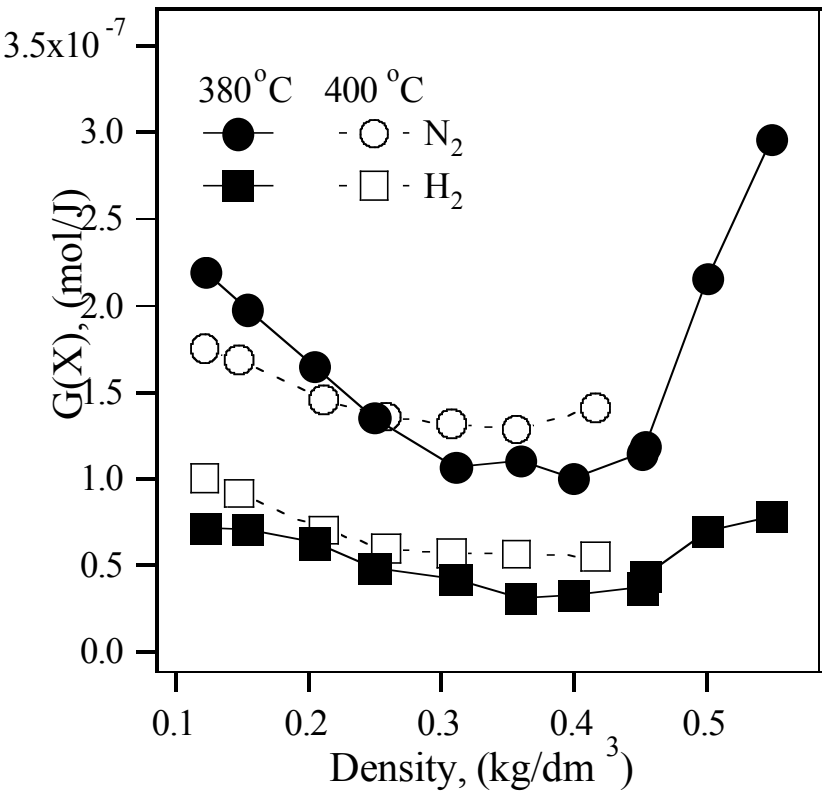

Figure 1.2B. Beta radiolysis G-values for Phenol/N_2O as a function of density in supercritical water.

Table 1.2B. G values at 380°C

Density (kg dm^{-3})	G(X) $\times 10^{-7}$ (mol J^{-1}) in 0.01 m PhOH		Density (kg dm^{-3})	G(X) $\times 10^{-7}$ (mol J^{-1}) in 0.02 m EtOH-d6		
	H_2	N_2		H_2	HD	N_2
0.1229	0.71	2.19	0.1218	2.16	5.26	3.74
0.1542	0.70	1.97	0.1617	1.67	4.54	2.59
0.2045	0.62	1.64	0.1980	1.39	4.01	1.76
0.2501	0.48	1.35	0.2567	1.24	3.36	1.52
0.3116	0.42	1.06	0.2934	1.07	2.83	1.42
0.3599	0.30	1.10	0.3639	0.89	2.57	0.94
0.4004	0.32	0.99	0.4018	0.77	2.43	1.25
0.4524	0.36	1.14	0.4540	1.03	2.92	2.05
0.4547	0.43	1.18	0.5126	1.06	3.04	4.07
0.5010	0.69	2.15	0.5430	1.10	2.83	4.68
0.5501	0.77	2.95	-	-	-	-

Yields of $(e^-)_{aq}$ (as N_2) and H_2 from the phenol system are shown in figure 1.2B as a function of density for fixed supercritical temperatures of 380°c and 400°C. Yields of both species drop to a minimum around 0.4g/cc density, and then increase again at lower density. Similar plots of the H atom (as HD) yield and H_2 from the EtOH-d5 system are shown in figure 1.2C. A minimum in yields at around 0.4g/cc is also found. The interesting feature here is the very dramatic rise in H atom yield as the density decreases at both temperatures.

Table 1.2C. G values at 400°C

Density (kg dm^{-3})	G(X) $\times 10^{-7}$ (mol J^{-1}) in 0.01m PhOH		Density (kg dm^{-3})	G(X) $\times 10^{-7}$ (mol J^{-1}) in 0.02m EtOH-d6		
	H_2	N_2		H_2	HD	N_2
0.1223	0.99	1.74	0.1211	2.06	3.14	2.24
0.1485	0.91	1.68	0.1518	1.86	3.15	1.95
0.2124	0.70	1.45	0.2124	1.73	2.81	1.81
0.2594	0.59	1.35	0.2594	1.54	2.49	1.67
0.3090	0.62	1.31	0.3090	1.32	2.29	1.61
0.3574	0.56	1.28	0.3574	1.32	2.22	1.60
0.4174	0.54	1.40	0.4094	1.33	2.35	1.51

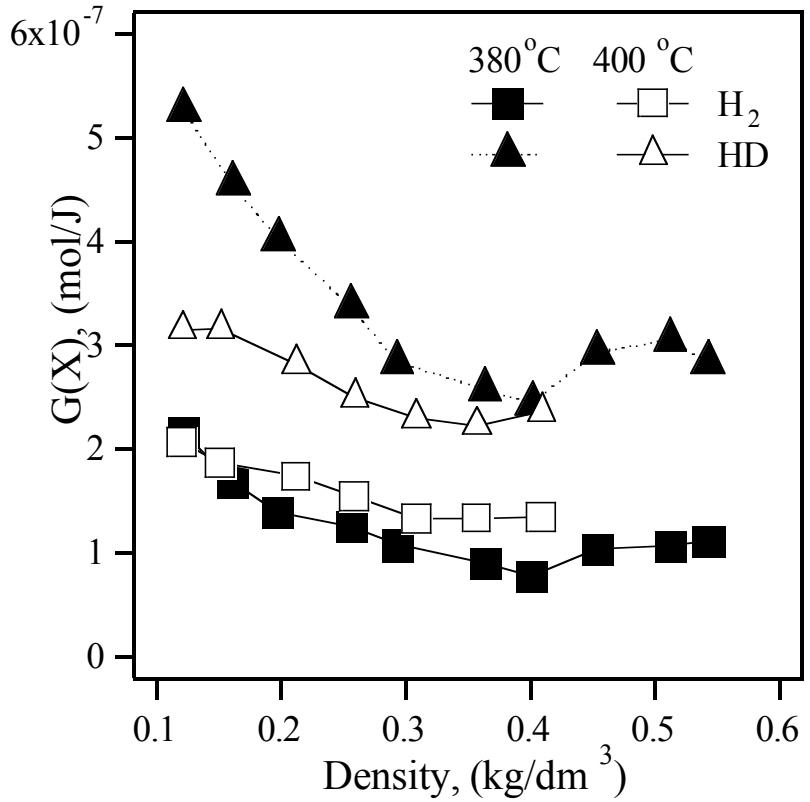

Figure 1.2C. Beta radiolysis G-values for ethanol-d5/N_2O as a function of density in supercritical water.

Behavior of $(e^-)_{aq}$, H atom, and H_2 yields in the two scavenger systems at 380°C is combined on figure 1.2D. It can be seen that the apparent H_2 yield in the ethanol d-5 system is nearly twice the yield in the phenol system. This is because of reaction (5) already mentioned above. We believe the phenol system gives a correct estimate of the H_2 yield. To get correct H atom yields at high temperature, we should use the formula

$$G(H) = G(HD, \text{ethanol-d5}) + G(H_2, \text{ethanol-d5}) - G(H_2, \text{phenol}).$$

As noted in the introduction, the object of modeling the chemistry is ultimately to determine the yield of product H_2O_2 and H_2. H_2O_2 represents the combination of two oxidizing OH radicals. H_2 represents the combination of two reducing radicals ($(e^-)_{aq}$ or H). From the measurements shown above we are able to determine a total yield of reducing equivalents, as

$$G(\text{red}) = G((e^-)_{aq}) + G(H) + 2\,G(H_2)$$

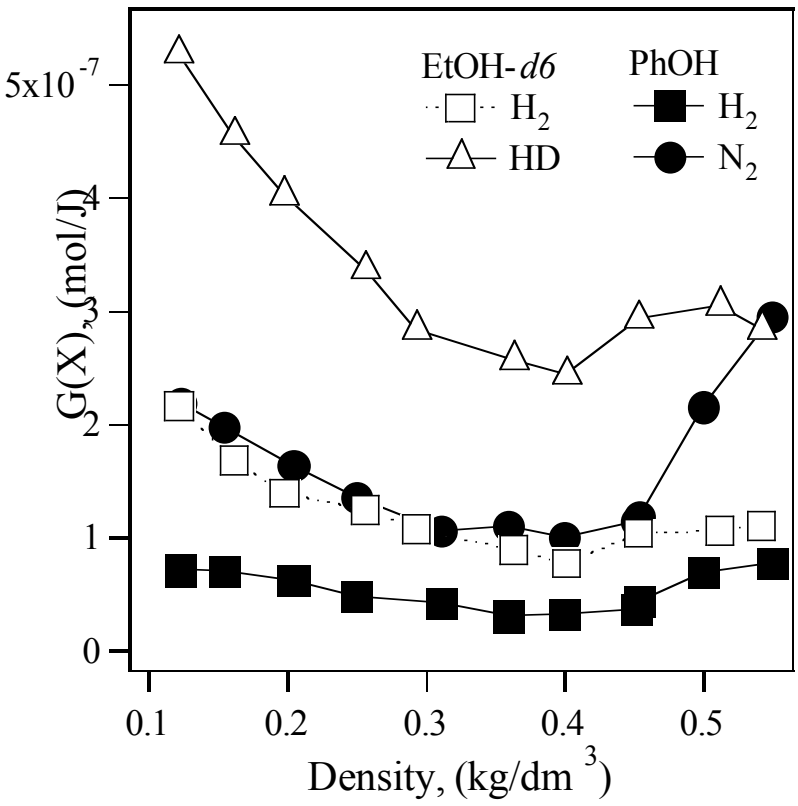

Figure 1.2D. Beta radiolysis G-values at 380°C as a function of density in supercritical water for both EtOH-d5 and Phenol systems.

By mass balance, this must also equal the yield of oxidizing equivalents, and the yield of water dissociation:

$$G(red) = G(-H_2O) = G(ox) = G(OH) + 2\,G(H_2O_2)$$

In Figure 1.2E we plot both the water dissociation yield and the corrected H atom yield as a function of density for 380°c and 400°C. In Figure 1.2F we plot both of these functions as vs. the temperature for 250 bar pressure. Two things become obvious from these plots. First, the total dissociation yield for water has increased a factor of over two, in going from room temperature to low density supercritical fluid. Second, the fraction of dissociation due to H atoms has increased dramatically in the low density fluid.

What do the numbers mean? Recalling the maximum possible G values for dissociation of water, on the order of 19 molecules per 100eV, we see numbers in supercritical fluid at 380°C on the order of 8 to 10 . So the prompt efficiency of water dissociation approaches 50% under these conditions. What is the net G value for production of H_2 and H_2O_2 after all recombination under these conditions? This depends on the efficiency of the cross reaction H + OH → H_2O relative to the faster of the homogeneous recombinations H + H → H_2 and OH + OH→ H_2O_2. In all probability H + H → H_2 is much faster than H + OH → H_2O in supercritical water. This will favor the H_2 and H_2O_2 products over the recombination to reform H_2O. Roughly speaking, the G value for H_2O_2 production should lie in the range ¼ to ½ of the G(-H_2O) that we have deduced here.

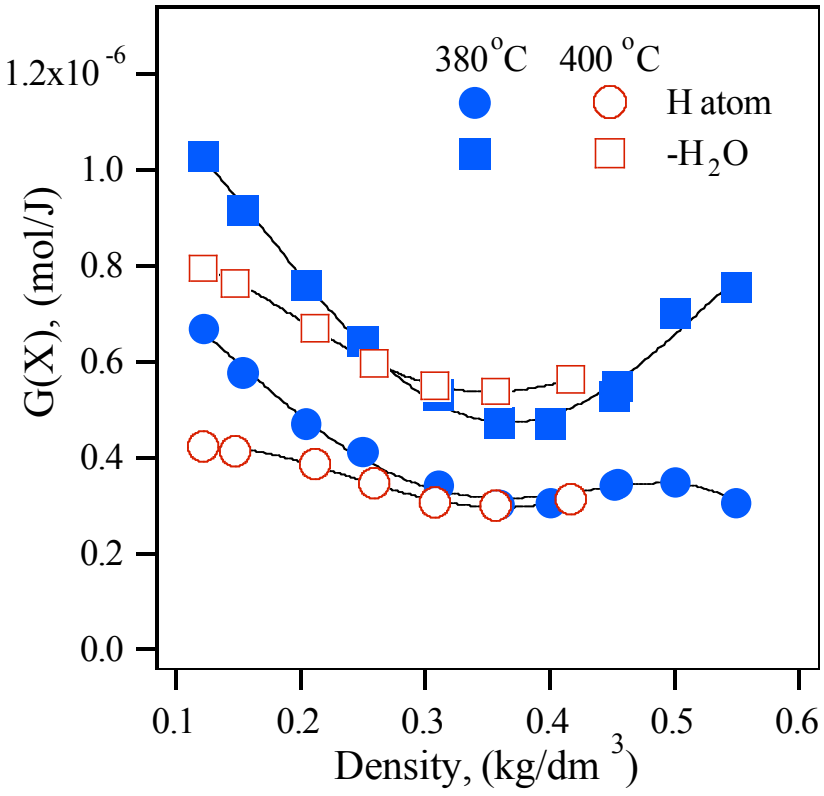

Figure 1.2E. Water dissociation yield and corrected H atom yield vs. density.

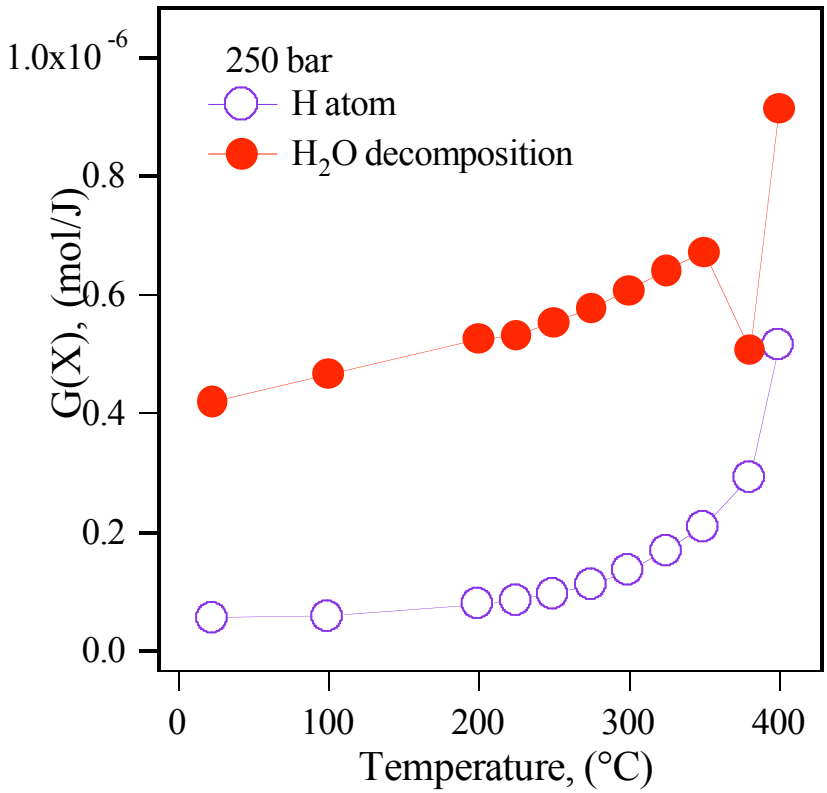

Figure 1.2F. Water dissociation yield and corrected H atom yield vs. temperature.

2. Neutron Radiolysis Yields

2.1 Experimental Description

The experiment used to measure neutron/gamma radiolysis product yields consists of a supercritical water loop inserted into the nuclear reactor at the University of Wisconsin and associated chemical analysis equipment [8,9]. Prior to initial experimentation, a rigorous safety analysis was performed that included radioactive isotope production, a radiation level analysis, a radiation survey, and reactivity stability of the reactor.

The University of Wisconsin Nuclear Reactor (UWNR) is a 1 MW TRIGA (Training, Research, Isotopes, General Atomic) reactor equipped with neutron irradiation experimental facilities including in-core sample positions, a pneumatic tube, three hydraulic irradiation tubes ("whale tubes"), a thermal column with an irradiation tube, and four beam. Of primary interest to this project, the beam ports are metal (aluminum in the pool, steel in the shield) tubes that go from the beam port floor, through the concrete shield of the reactor, and to the edge of the core grid box in line with the center of the core. They are made two separate coaxial sections, a 15.24 cm (6 in) diameter section from the core approximately 2.5 m long and a 20.32 m (8 in) diameter section 0.9 m long to the outside of the shield. When not in use, the beam ports are filled with high density concrete shielding plugs and a lead gamma shutter to limit radiation levels on the beam port floor. A cut-away diagram of the reactor can be seen in figure 2.1-1 and a beam port drawing can be seen in figure 2.1-2

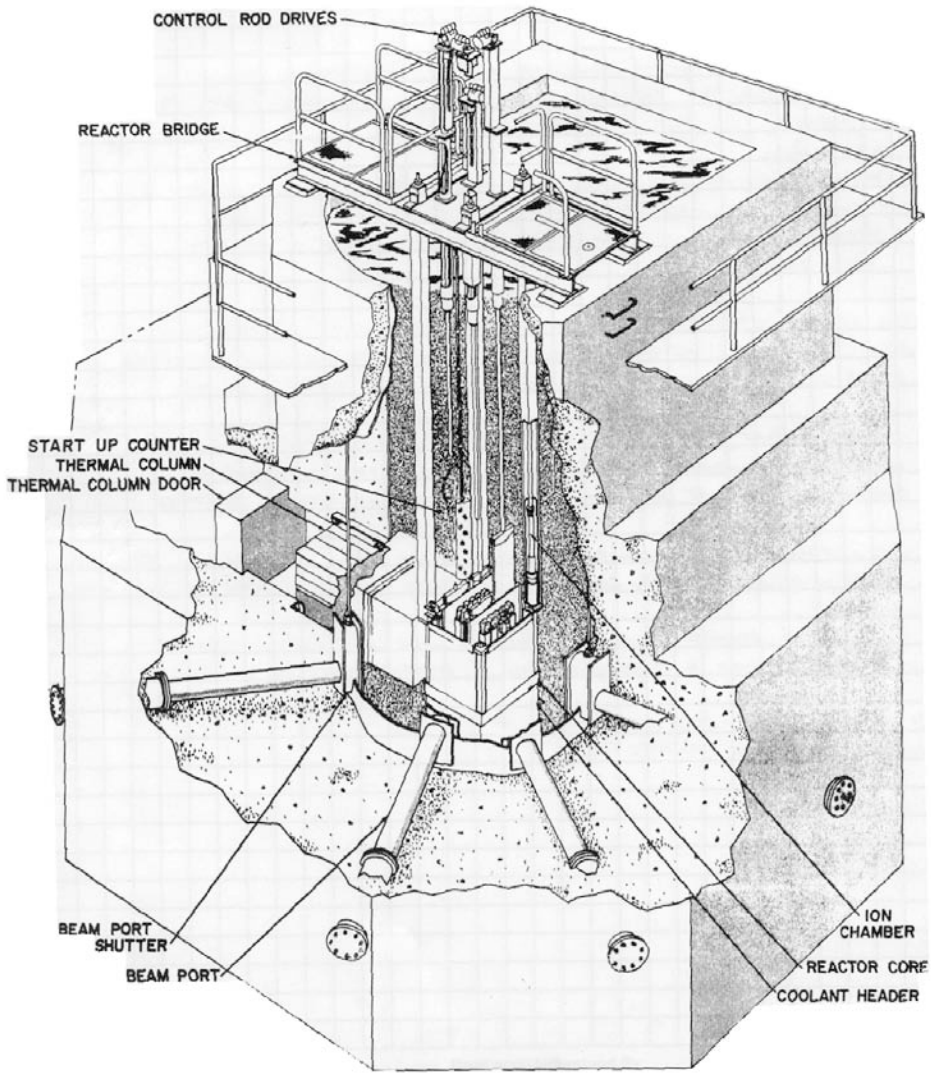

Figure 2.1-1: A schematic drawing of the UWNR. Note the beam ports extend all the way to the edge of the core, but are cut away for viewing.

The reactor core consists of 23 fuel bundles (91 elements) with 5 graphite reflectors on each side. The fuel is TRIGA-FLIP fuel enriched at 70% U-235 in the form of U-$ZrH_{1.6}$ clad in 20 mill stainless steel and uses 1.5 wt% erbium as a burnable poison. The core is cooled by natural convection with demineralized light water. The second beam port (second from the right

on **Figure**), where the experiment is installed, connects to the core grid box opposite the north set of graphite reflectors at an angle of 60^{o} and is aligned with the center of the core.

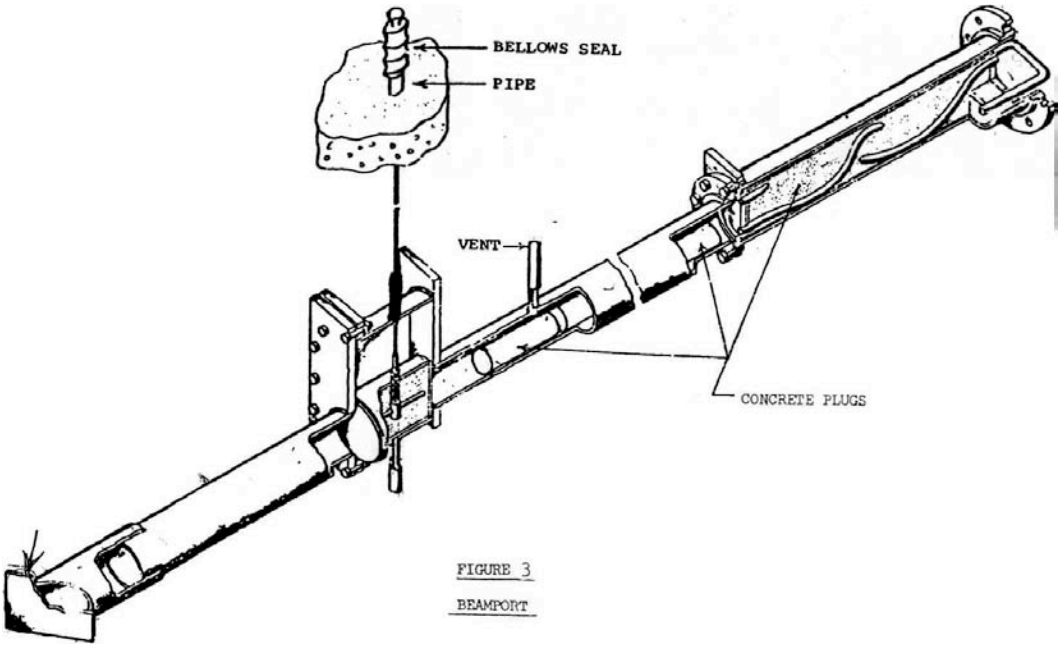

Figure 2.1-2: Schematic of a reactor beam port. The outer section has a larger diameter to avoid streaming of radiation around the shielding in the inner section.

In addition to the beam ports, the pneumatic tube system has been used as a benchmark tool for simulation software. This experimental facility transports samples to a position near the reactor core and directly below the beam port used for this experiment. It has the ability to deliver samples for precise irradiation times as short as one second.

Experimental data is normally desired at full power in the automatic mode of operation. In this mode, power level is maintained with a servo amplifier that compares a neutron signal from compensated ion chambers to the desired power level and moves a control blade to meet the demand (usually transient rod). Typically, it takes 20 minutes for the reactor to reach a steady state of gamma radiation from startup.

2.1.1 MCNP Model

To further the understanding of the radiation inside of the experimental apparatus at full power, a model of the reactor has been constructed in MCNP (Monte Carlo N Particle transport code). This model includes the core, pool, reflectors, structural material, and the reactor shield including the beam ports and inserted apparatus. To obtain appropriate statistics, the irradiation volume was modeled as a cylinder of water. A plot of the model can be seen below in figure 2.1-3.

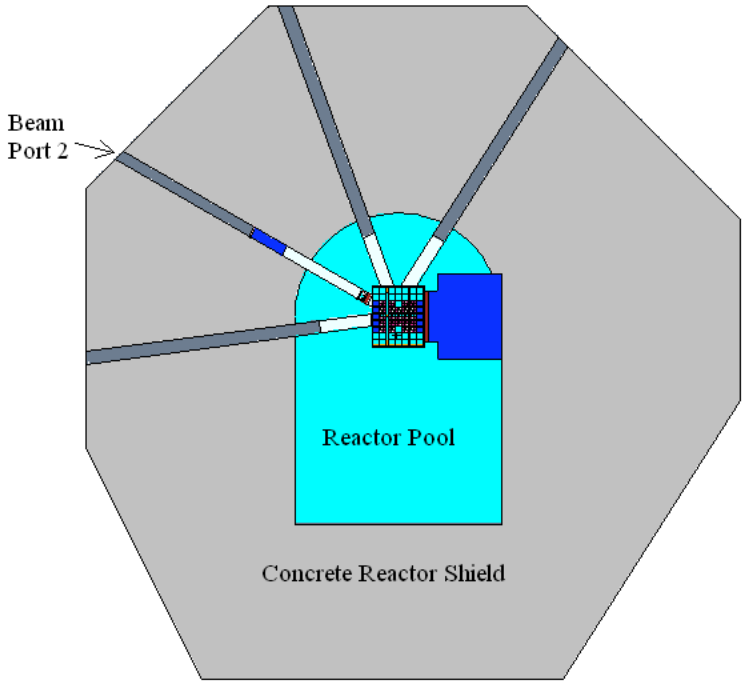

Figure 2.1-3: The MCNP model of the reactor with the experiment inserted.

The MCNP model has been used to obtain certain physical quantities of the reactor such as the ratio of energy deposition to sodium activation in the loop. This quantity is necessary to calculate the neutron energy deposition calibration. It has been benchmarked with various methods, including foils in the beam port to compare neutron fluxes at different energies. More benchmarking is planned as the model continues to grow over time.

2.1.2 Water Loop Apparatus

The experimental apparatus used in the neutron radiolysis experiments is shown in figure 2.1-4 and is similar to the beta gamma system described in section 1. The apparatus is designed to fit into beam port two of the University of Wisconsin Nuclear Reactor (UWNR). Several factors were considered in the design of the test loop; a high neutron flux requiring the irradiation volume to be as close as possible to the reactor core, constant temperature within 0.1^{o}C during the irradiation time, and sufficient radiation shielding for experiment operators. These criteria lead to a fairly complex design including heating, temperature monitoring, pressure and chemistry control, graphite moderation, boral neutron absorption, lead gamma shielding and water radiation shielding.

Figure 2.1-4: The apparatus outside of the reactor.

The apparatus can be divided into 4 main sections, (1) the irradiation volume/void and neutron shielding section, (2) the lead gamma shield section, (3) the voided heating section and (4) the water shielding section (figure 2.1-5).

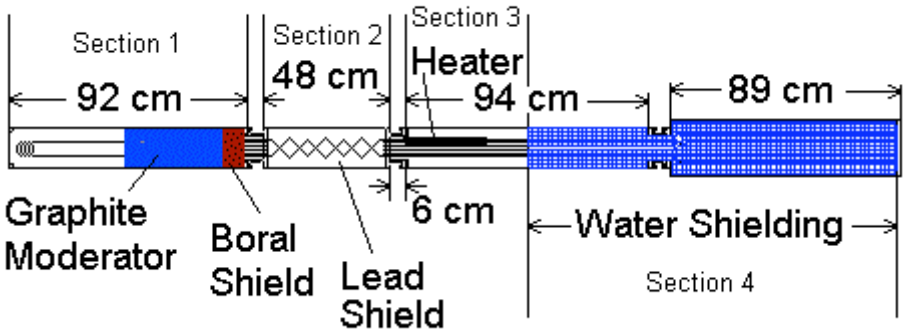

Figure 2.1-5 : The apparatus design, not to scale.

2.1.2.1 Section 1

Nearest the reactor core, section 1 is a voided section with the irradiation volume and neutron moderator and shielding. In this portion four graphite blocks 7.62 cm (3 inches) long each and one 5.04 cm (2 inches) long were stacked to create a neutron moderator. The cylindrical blocks were machined to allow six feed through ports in a helical pattern to prevent neutron streaming. Behind the graphite a 2.54 cm (1 inch) section of 8 0.318 cm thick boral plates are stacked to form a neutron shield. One of the six feed-throughs allows a 0.317cm (1/8 inch) OD 0.051 cm (0.020 inch) wall hastelloy C276 tube to enter into the irradiation section. This tube carries preheated pressurized water from section three through a gamma shield, into section one, and into the irradiation volume. The second of the six feed-throughs serves as an outlet for irradiated water. The remaining feed-throughs allow for thermocouples to monitor the inlet and outlet temperature of the irradiation volume (k-type thermocouples were inserted through a 0.318 cm (1/8 inch) Swagelok compression tee that connected the hastelloy C276 tube to the titanium irradiation volume), aluminum wires for ohmic heating of the irradiation section and for tubes to evacuate the section to reduce Ar-41 production and to minimize thermal convection to the inner walls of the aluminum tube.

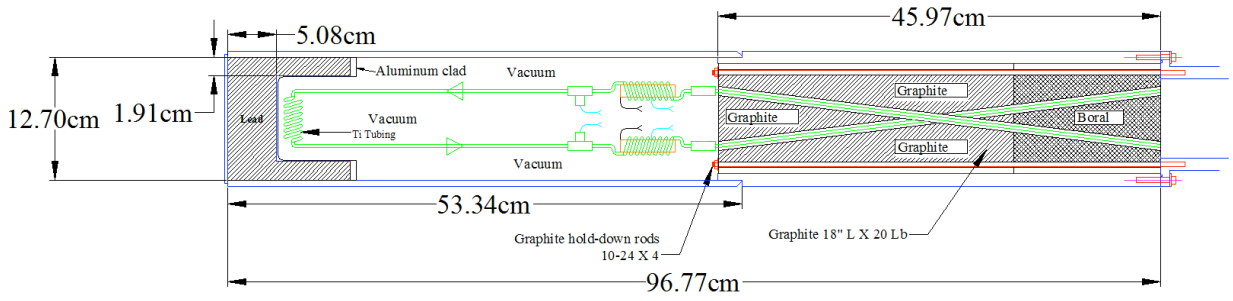

Figure 2.1-6 Section 1 of the apparatus.

The outer structure of section 1 is constructed from a 91.7 cm long 6061T6 aluminum tube with an outer diameter of 12.7 cm (5 inch) and wall thickness of 0.635 cm (0.25 inch). The reactor side end is sealed with a 0.318 cm aluminum 6061T6 aluminum plate welded to the tube end. The rear portion of this section is sealed to an aluminum junction piece which connects section 1 to section 2 with a 0.159 cm (1/16 inch) o-ring seal and series of 12 ¼ -20 – 316 stainless steel bolts. The rear half of this section was constructed with a slightly thicker aluminum tube 1.27 cm thick with an 11.43 cm (4.5 inch) ID.

2.1.2.2 Section 2

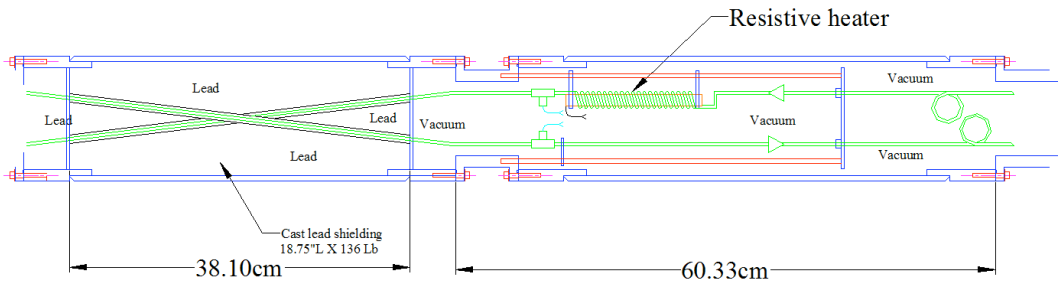

Figure 2.1-7: Sections 2 and 3 of the apparatus.

Section 2 of the test loop is 48.3 cm long and contains a lead gamma shield with helical paths for the feed-throughs. This section is constructed with six 0.95 cm (3/8 inch) tubes welded

to two end plates and then cast with lead. The joint in the front of section 2 (between sections 1 and 2) contains a small heater to recover heat lost in the lead section.

2.1.2.3 Section 3

Section 3 (94.7 cm) contains the first stage of heating and first stage of water shielding. The water is heated above the desired irradiation temperature by the cartridge heater to accommodate energy loss during transport through the lead and carbon/boral shielding. The rear half of section 3 and the entire volume of section 4 are filled with distilled water for neutron shielding and to reduce the temperature of the irradiated sample water back to room temperature for analysis.

2.1.2.4 Section 4

Section four is constructed out of a 19.8 cm (7.8 inches) OD 1.27 cm (0.5 inch) thick aluminum 6061T6 tube. The outside diameter change fits the change in the beam port diameter, which was designed avoid streaming of radiation around the outside of shielding in the smaller diameter section. The end of the test loop is welded to a 1.27 cm (0.5 inch) thick flange and is sealed with a 0.318 cm (1/8 inch) o-ring face seal to the reactor beam port flange.

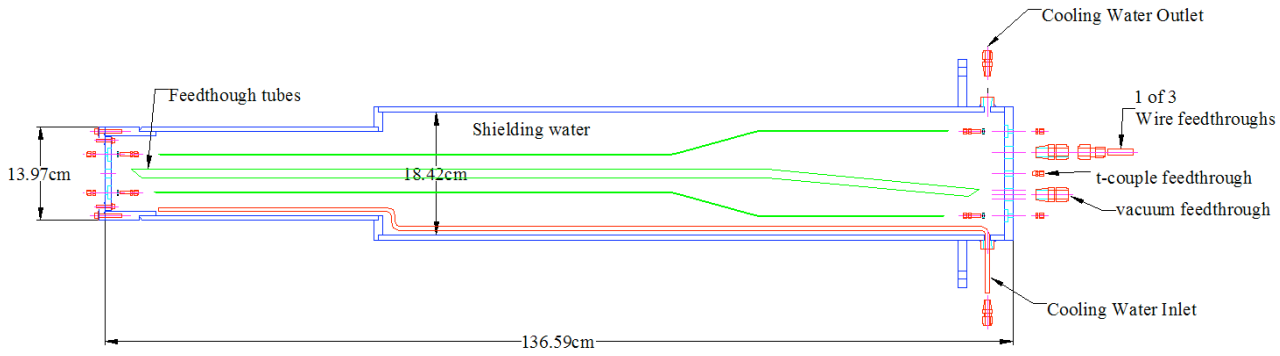

Figure 2.1-8 Section 4 of the apparatus

2.1.3 Thermo-hydraulics

Water enters the apparatus in section 4 in 0.159 cm ($1/16^{th}$ inch) OD, 0.108 cm (0.05 inch) ID hastelloy C276 tubing and travels through the water shielding to the main cartridge heater in section 3, where it is heated above the final desired temperature. After leaving the heater, it travels through the lead shielding section and into the secondary cartridge heater where heat lost in the lead section is recovered. It continues through the neutron shielding and into the 0.318 cm ($1/8^{th}$ inch) OD, 0.155 cm ID titanium irradiation volume (see section 0). After irradiation, it returns to 0.159 cm OD hastelloy C276 tubing, through neutron shielding, lead gamma shielding, and water shielding to the exit of the apparatus.

2.1.4 Heaters

The first stage of heating utilizes a cartridge heater with 1.5 cm diameter and approximately 20 cm long wound tightly with a 0.159 cm (1/16 inch) diameter hastelloy C276 tube. The tubing is wrapped around the heater about 80 times and has a straight length of 5 m. The heated water temperature is measured at the inlet, middle and outlet of the cartridge heater section, and is controlled to less than 570 C for water and 450 C for water with N_2O to avoid thermal breakdown of water or N_2O. To avoid conductive contact with the surroundings, the heater and tubing are wrapped with alumina-silica fiber insulation. This heater is controlled by hand by adjusting a Sorensen DCR 150-6B DC power supply.

Depending on temperature, the water will lose up to 200 C between the first heater and the irradiation volume. Originally, this heat loss was made up with ohmic (DC current) heating through the tubing between the lead and the irradiation volume, but since ohmic heating is also used in irradiation volume, the two DC currents used to heat the tubing interfered with each other. The DC current heating was thus removed and a small secondary cartridge heater was

used. This second heater is approximately 1.5 cm in diameter and 3 cm in length. It again is limited by thermal breakdown of water, not internal limits or limits of the hastelloy C276 tubing. The second heater is also wrapped with alumina-silica fiber insulation. The heater is controlled by adjusting a rheostat from 0-80% of 120 V AC.

The final stage of heating is a DC current that runs through the entire irradiation volume. Typically, current is up to 20 A and voltage is up to 15 V for high temperature operations. Heating of the wiring has to be taken into account due to the high power loss caused by the high current, especially since aluminum wire was used near the irradiation volume to avoid neutron activation. Fluctuations in resistivity of the tubing caused by temperature in addition to power fluctuations tend to vary the current and voltage through the tubing, even after a steady state temperature is reached. The DC current heating is controlled by hand via a NJE SY 36-30-M DC power supply. More detail on the irradiation volume can be found in section 0.

2.1.5 Vacuum System

Within the apparatus where there is no shielding, a vacuum is pulled by a rotary vane pump. Pressure, measured at the inlet to the apparatus is normally kept below 267 Pa (2 torr). Without the vacuum, it becomes impossible to keep water at a constant temperature through the irradiation volume.

2.1.6 Irradiation Volume

Irradiation volumes have consisted of different materials and size tubing. The first irradiation volume was made of 1 meter of hastelloy C276, 0.3175 cm OD, 0.2159 cm ID wrapped in a single square shaped coil that extended all the way to the end of the apparatus (no lead shield was planned at the time). This irradiation volume was limited to 24 MW-hours of

irradiation or 24 hours of experimentation time due to activation of the high concentration of cobalt (<0.77% nominal).

The second irradiation volume was made of inconel, chosen for its strength at high temperatures and corrosion resistance along with a smaller concentration of cobalt. The dimensions of this irradiation volume were nearly identical to the hastelloy C276 setup. It was replaced after a decision was make to construct the lead shield. A picture can be seen of the design of the first two irradiation volumes in figure 2.1-9, as well as the inlet and outlet thermocouples.

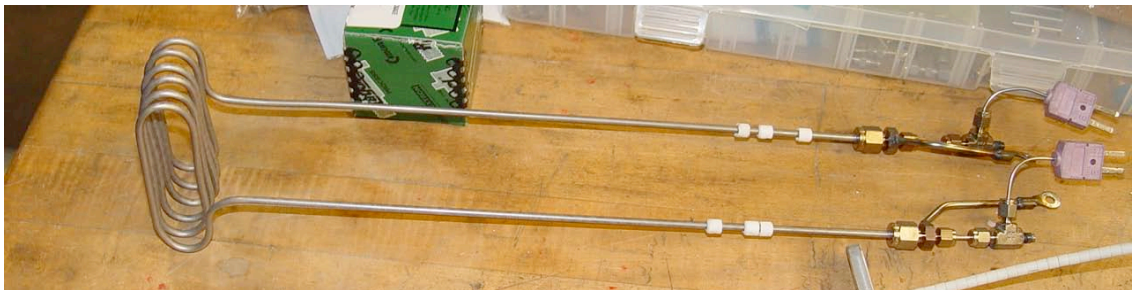

Figure 2.1-9: The first irradiation volume design

The third and fourth irradiation volume, designed to maximize the residence time of the sample water near the core of the reactor while allowing room for a lead shield, were made of 0.3175 cm OD, 0.155 cm ID titanium tube with 2 meters of length arranged in a 7 cm long double coil (shown in figure 2.1-10). Titanium was chosen for the irradiation volume for three reasons, minimization of radiation induced chemical wall reactions, minimization of neutron activation, and structural strength. The new irradiation volume only replaced the 1/8 inch section of the first irradiation volume, and the same thermocouples as seen in 2.1-9 were used. Since the coil has a heating current running through it, it is formed so that the tubing does not contact itself, causing a short circuit. Approximately 100 watts of power is used to maintain the sample

water at a constant temperature (less than a 0.1 C temperature difference between thermocouples). The first titanium irradiation volume was replaced because after maintenance, a short circuit did form between the coils, which caused a leak.

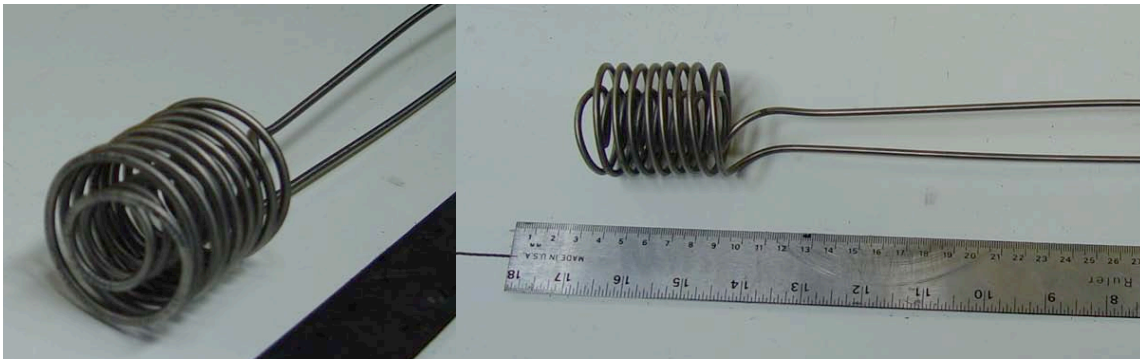

Figure 2.1-10: Photographs of the second titanium irradiation volume.

2.1.7 Neutronics

Preliminary MCNP analysis suggested that there would be sufficient fast flux to produce detectable amounts of radiolysis for the experiment. Following experimentation, it was found that the gamma dose was also significant, and the neutron to gamma energy deposition ratio would have to be increased. The neutron flux determined by MCNP can be seen as a function of position in figure 2.1-11. This result along with the dimensions of the irradiation volume showed that >99% of neutron fluence received is in the section of the irradiation volume where temperature is controlled.

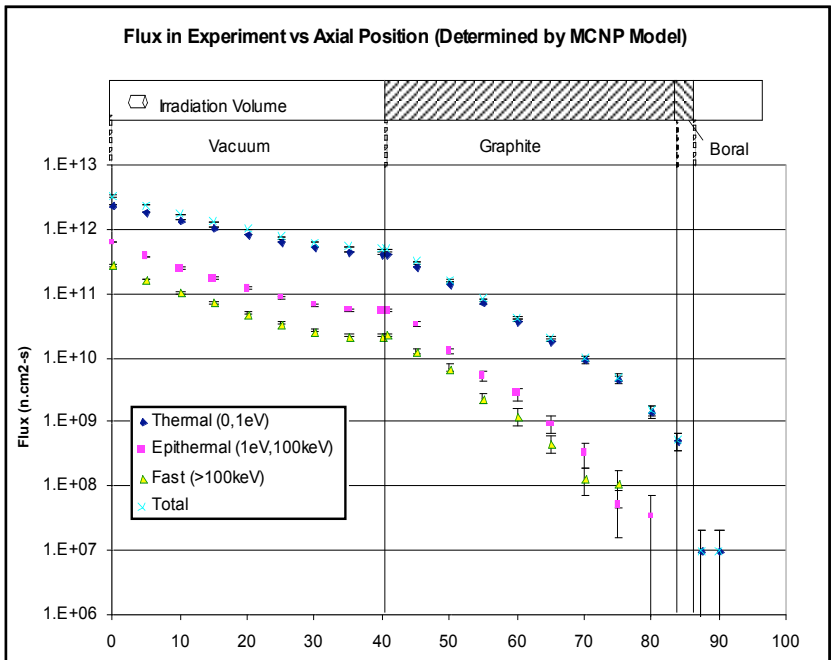

Figure 2.1-11: Neutronic analysis of the experiment as a function of axial distance from the end of the apparatus.

2.1.8 Lead Shield

After experimentation and further MCNP analysis, it became evident that a large portion of the radiation energy deposition was from gamma radiation. In order to enlarge the neutron contribution to total energy deposition, a lead gamma shield between the core and the irradiation volume was developed. Following an MCNP analysis, an idealized design was made with respect to shape, size, and thickness taking the irradiation volume size into account. The final constructed design can be seen in figure 2.1-12.

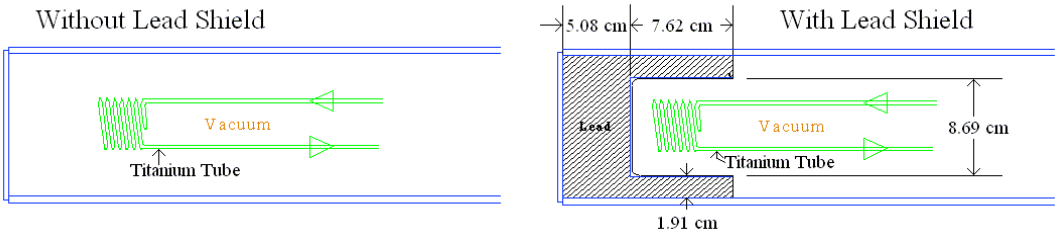

Figure 2.1-12: The irradiation volume in the end cap with and without the lead shield.

Further MCNP analysis predicted that the shield would reduce gamma energy deposition to 19.5% of the original value and neutron energy deposition to 69.9% of the original value. This resulted in a predicted 1.84 factor improvement in the neutron fraction of energy deposition.

2.1.9 Water Preparation Components

Water for the experiment is prepared by filtering distilled water through an Elga Purelab Classic Filter to produce high purity (18.2 MΩ-cm) water, minimizing the neutron activation of contaminants and the potential for flow obstruction in capillary tubing. Liquid and/or gaseous chemical scavengers such as nitrous oxide and ethanol D6, which scavenge aqueous electrons and hydrogen radicals respectively, are added to the water to create stable chemical species to be measured at the outlet. Other dissolved gases are sparged out using gases that aren't measured in analysis such as helium. Solutes that would activate to radioactive gases such as argon are avoided. Liquid scavengers are mixed into the water solution inside of glass or stainless steel bubbling reservoirs. All tubing in the system is stainless steel 316L or hastelloy C276 to avoid the infusion of oxygen that would occur with plastic tubing.

2.1.10 Pumps

Two constant flow rate high performance liquid chromatography (HPLC) pumps (Chrom Tech Inc P1100), capable of flow rates of 0.1-20.0 mL/min, are used to control the total flow rate

through the system. The relative concentrations of the dissolved scavengers are controlled by adjusting the flow rates of these pumps, which are connected to different chemically prepared water reservoirs.

For low flow rates of water with dissolved N_2O, cavitation of the HPLC pumps has lead to adding syringe pumps to the system. The pumps used were ISCO 260D syringe pumps, capable of flow rates of 0.001 mL/min to 107 mL/min at pressures up to 517 bar. The water reservoir for these pumps is 266.05 mL, meaning that they need to be refilled after every 266.05 mL of water pumped, unlike the HPLC pumps that take water from an external reservoir. The syringe refill flow rate must be low to keep N_2O from being pulled out of the solution.

2.1.11 Capillary Tubing and Pressure Control

After water exits the irradiation volume, it returns to atmospheric pressure through stainless steel capillary tubing. The pressure is controlled by the viscosity of the water in the capillary tubing, controlled via a constant temperature bath. It is important to avoid turbulent flow (approximately 43 C) in the tubing because the pressure drop has a discontinuous drop at the boundary of turbulent flow. Pressure in the system is measured at the inlet and outlet of the apparatus by two Siemens Sitrans P pressure transducers. The typical pressure drop through the entire piping system at a flow rate of 10 mL/min is on the order of 240 kPa, less than 1% of system pressure (25 MPa). The pressure in the irradiation volume is determined by a weighted average taking into account the length of tubing into and out of the irradiation volume. After the irradated water is depressurized through the capillary tube back to atmospheric pressure the sample is sent to the chemical analysis system.

2.1.12 Sample Chamber

The sample chamber normally transports sample water from the inlet through the water valve and into the "water bypass" flow to waste as seen in figure 2.1-13. When a sample is taken, the water valve is simply turned to collection position, and sample water flows into the water sample collection volume, while the argon sparging gas is in bypass mode (so no Ar is bubbling through sample during collection). The sample volume is approximately 15 mL in volume, but typically, a 10 mL sample is taken as room is needed at the top of the volume for the bubbling caused by sparging. This sample is measured by timing the flow into the chamber and using a calibrated flow rate.

When a sample is collected, the gases formed in the sample are removed by sparging with ultra high purity argon gas. The mixture is sparged until all formed gases are removed and the sample becomes saturated with argon. At this point, the gas flow is returned to bypass, and the water valve is turned to dump (this is a 3-way valve, and both "water flow in" and "water sample flow" go to waste). The sample is pushed out against the flow of water in by the pressure of the argon gas flow (both water in and sample are open to waste).

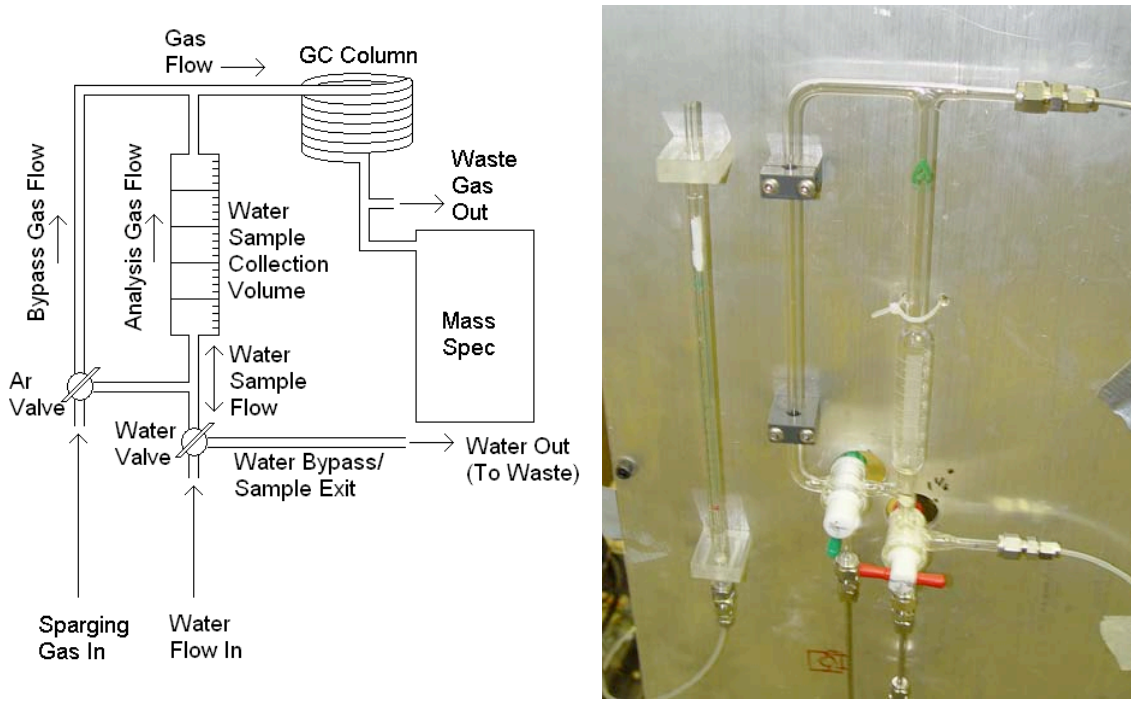

Figure 2.1-13: The water sample chamber and a schematic of flows.

2.1.13 GC Column

Following sparging, the gas mixture is separated from water vapor in a gas chromatography (GC) column filled with molecular sieve A4 beads according to the reactivity of the gas. This not only prevents water from entering the analysis, where it would interfere with hydrogen results, but also prevents nitrous oxide (N_2O) from reaching analysis where it would interfere with nitrogen analysis. The GC column must be baked out at high temperature with gas flowing through to remove water after every 50-100 samples or it will not stop water or nitrous oxide.

2.1.14 Mass Spectrometer

The gases flowing out of the GC column are sampled through a 3 m long 0.05 mm ID flexible fused silica tube (Alltech 602035) into a vacuum chamber. The capillary tube keeps the

chamber at approximately 7.5E-4 Pa (5.5E-6 torr). The sample gas flows around the tubing (only a small fraction is analyzed) and the gas that does not flow into the vacuum chamber instead goes through a flow meter (to assure constant flow throughout the day), and is released to atmosphere. A Pfeiffer QMS 200 mass spectrometer is used to detect gases inside the chamber, and has sufficient resolution to separate isotope gases, but not different gases of the same mass.

The data for this experiment is taken by measuring gaseous samples removed from liquid. The mass spectrometer ionizes gas and measures ion current of a particular gas by applying electric and magnetic fields. The physical quantity being measured is the mass/electric charge ratio, meaning water that is singly ionized will be measured in channel 18, and water that is doubly ionized will be measured in channel 9. The ionization process also has the ability to break molecular bonds, which would thus measure a sub-product of the gas in the chamber.

2.1.15 Mass Spectrometer Techniques

When a sample is sparged, it creates a curve similar to but smaller than the calibration curve in **Figure**. The method of analysis is to integrate the curve and subtract out the baseline. This is done inside of the Quadstar program by selecting a region of interest, and selecting the integral data. The integrated value has units of amps-seconds.

2.1.16 Mass Spectrometer Calibrations

The mass spectrometer is calibrated by relating integrated current to moles contained in a sample as described in the analysis section of this paper. This calibration is performed by running water saturated with 89.9% nitrogen and 10.1% hydrogen (our calibration mixture) in samples of approximately 10 mL (actual volume was measured with a stopwatch and recorded). An example of a calibration peak can be seen in figure 2.1-14. The calibration is run both at the beginning and the end of the day (only the end of the day if syringe pumps are not available) and linear interpolation is used to determine the calibration for each sample as a function of time. The calibration changes due mainly to the changing conditions in the GC column and the decaying signal amplification of the electron multiplier, and will typically be 3% different between the beginning of a data run and the end (9 hours apart). The highest difference seen has been for H_2 and was measured to be 7.2% or 0.8%/hr. The highest difference for N_2 was 5.1%. The general trend of the calibrations is that the calibration coefficient goes up from day to day in a somewhat linear manner due to the electron multiplier. If it was desired that this affect be avoided from day to day, the high voltage to the SEM could be increased each day, but this would yield the same results as the current method and would be less efficient.

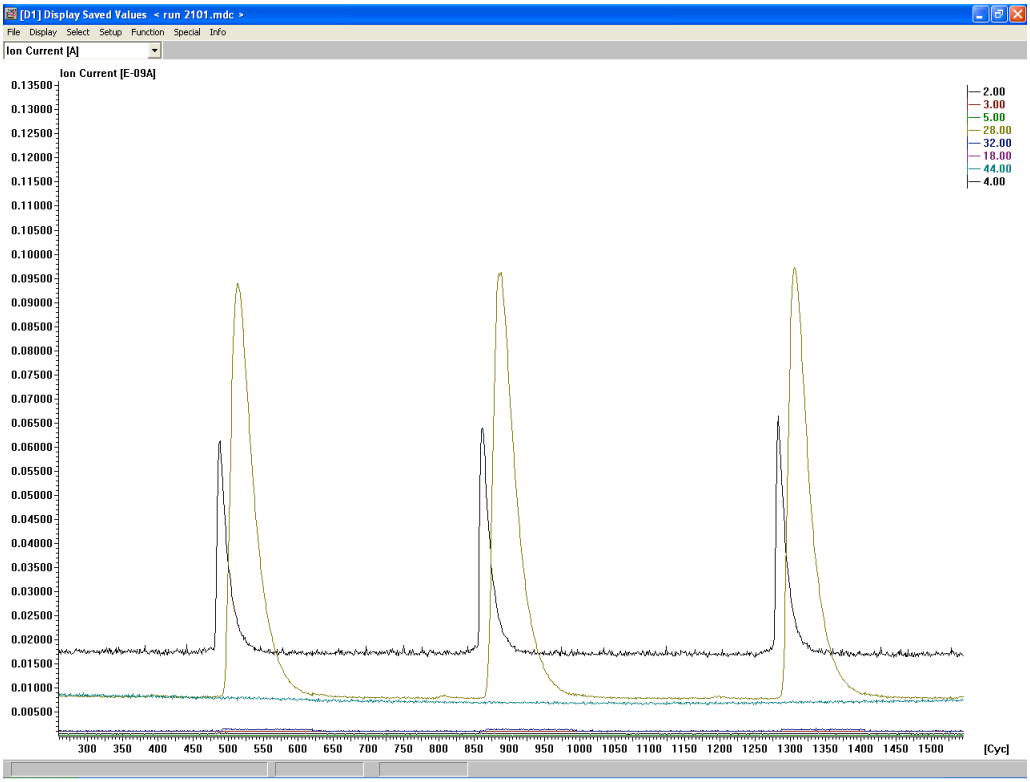

Figure 2.1-14: A calibration run with hydrogen (black) and nitrogen (yellow) peaks.

Each day, the argon sparging flow rate is controlled by hand, which can vary the calibration factor. Once the flow rate is set, it is checked throughout the day and receives minor adjustments. The calibration factor varies because the gas in the sample is removed faster as flow rate goes up, but only a fraction of the gas is sampled at any time. The result is that for a faster flow rate, there is a higher peak and a smaller integrated area while a slower flow rate will yield a broadened, lower peak with a larger integrated area. Ideally, a good signal to noise ratio yields the best signal, so a sharp peak is preferred. The value of 90-100 mL/min is preferred because it gives a sharp response, a large area and the sparging is a gentle bubbling (a violent bubbling should be avoided so that liquid sample does not enter the GC column).

The sparging gas flow rate was initially measured with a floating ball type flow meter. This flow meter was a 16 unit full scale glass tube, and the preferred argon flow of 100 mL/min

was at 4 units, or about ¼ full scale. This did not give sufficient precision to keep the sparging gas at a constant flow rate for a constant calibration factor, which could change up to 10-20% without a significant response on the meter. The flow meter was replaced with a 110 mL/min full scale digital read out flow meter due to the necessity of a high precision and accuracy for this experiment. The variation of calibration factor as a function of the numeric flow rate off the older flow meter can be seen in figure 2.1-15 below. Typically, a flow rate of 3.8-4.2 may be read at 4, depending on conditions.

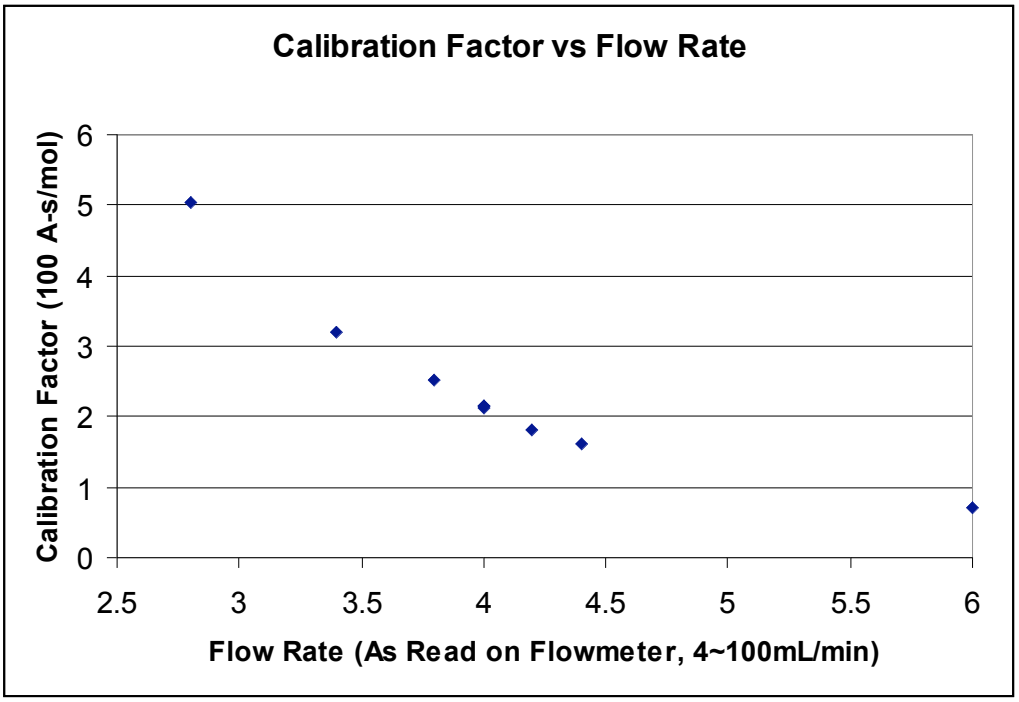

Figure 2.1-15: The variation in mass spectrometer calibration as a function of flow rate.

2.2 Radiation Energy Deposition Calibration and Results

In order to obtain the radiolysis yields as a function of the neutron dose the energy deposition in the water by radiation must be well known. In addition, since molecules of radicals formed per unit energy by neutrons alone is desired from data taken in a mixed field (neutrons

and gammas), not only must the radiation energy deposition be well known, but also the separate energy deposition of both neutron and gamma radiation. The gamma energy deposition data presented in section 1 can be used to subtract the radiolysis by gamma radiation with results from the Notre Dame Lab, and the remaining formation can be used to calculate G-values with the neutron energy deposition. A flow chart of this necessary information can be seen in figure 2.2-1.

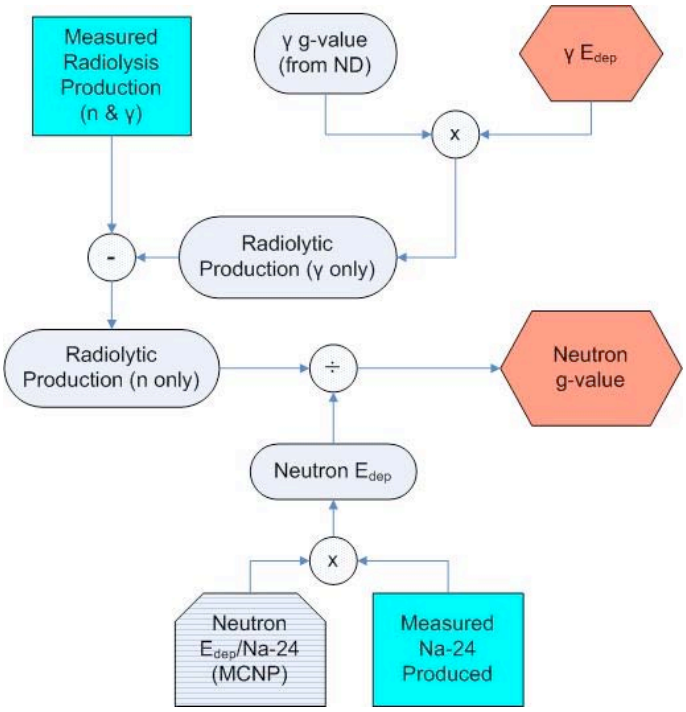

Figure 2.2-1: The necessary inputs to determine neutron g-value, the quantity that is desired. Red hexagons are unknowns, turquoise squares are experimentally determined values, horizontally striped polygons are simulation results and gray ovals are intermediary values.

2.2.1 Neutron Activation Analysis of Sodium-24

The MCNP model can tally neutron flux and energy deposition with different multipliers on a surface or through a volume. The results of the flux tally are in units of $\frac{neutrons}{cm^2 source\ neutron}$. The more contemporary unit of nv or $\frac{neutrons}{cm^2 s}$ is achieved by multiplying the first value by total source

neutrons/second in the entire reactor system. In the same manner, energy deposition from neutrons can be calculated as a function of position, and can be used to develop total energy deposition in the water. In order to perform this analysis, however, the position of the irradiation volume must be well known as well as the flow rate so that the energy deposition can be integrated over time and space. Since this is difficult to measure the exact position of the irradiation volume with good confidence, a different energy deposition technique was chosen to calibrate neutron flux involving neutron activation analysis of sodium. This method uses MCNP to calculate a ratio that does not change as a function of position over a small portion of geometry, the ratio of neutron energy deposition to Na-24 production in water containing sodium carbonate.

MCNP calculates flux in a "tally" that essentially counts each separate neutron as it crosses a boundary or is inside of a volume. Because it is counting flux one neutron at a time, it can calculate sodium-24 production one neutron at a time using the continuous sodium-23 cross section. This also eliminates the need for an accurate flux weighted sodium cross section.

In the same way, neutron energy deposition is calculated with a continuous energy transfer cross section and total neutron energy deposition is tallied. Using a combination of the sodium and energy deposition tallies, energy deposition (from mainly fast neutrons) can be calculated from an experimental production of sodium-24 (from mainly thermal neutrons). This calculation depends on MCNP predicting the correct energy distribution of neutrons, which has been benchmarked with fast/thermal neutron activation of foils.

2.2.2 MCNP Gamma Predictions

MCNP can also be used to track prompt gammas from fission and neutron interactions with material around the irradiation volume. Again, tallies can be made on gamma flux and

energy deposition. Preliminary results have shown, however, that MCNP is predicting less gamma energy deposition than is evident from room temperature radiolysis. A radiolysis experiment has been devised to experimentally determine the gamma energy deposition and further benchmark MCNP for gamma radiation if the problem can be accounted for.

2.2.3 Radiolysis Experiment

As mentioned in the beginning of this section, knowing an accurate value of gamma as well as neutron energy deposition is essential to this experiment. The flow chart in figure 2.2-1 can be adapted to be like figure 2.2-2, where neutron and gamma g-values at room temperature are determined from simulations with known inputs at room temperature.

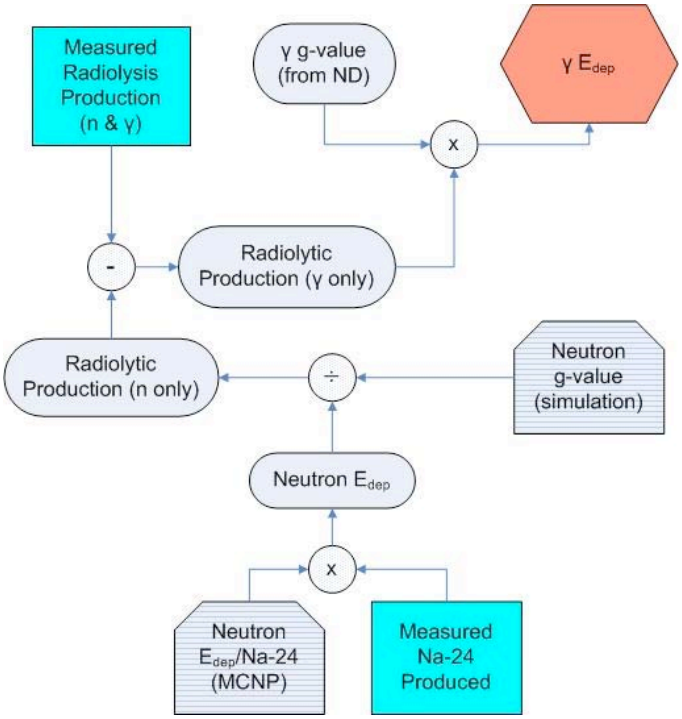

Figure 2.2-2: The necessary changes from Figure to determine gamma energy deposition at room temperature.

Simulated g-values are determined through Monte Carlo/independent reaction pairs (MC/IRP) simulation of water radiolysis with the same radiolytic conditions as the sample we

are using. For gamma radiation, this is simple because molecules formed per unit energy deposition is not a strong function of gamma energy spectrum. Neutron g-values are determined through a more rigorous analysis. The process begins with the determination of a fine group weighting neutron flux spectrum. This result is then used in NJOY, a nuclear data processing system, to generate H^+ and O^+ primary knock on atom (PKA) spectrums. The PKA spectrums are used with data and water conditions to calculate neutron g-value for the system with that neutronic spectrum. G-values calculated from MC/IRP of the ethanol-d6 solutions can be seen below in figure 2.2-3.

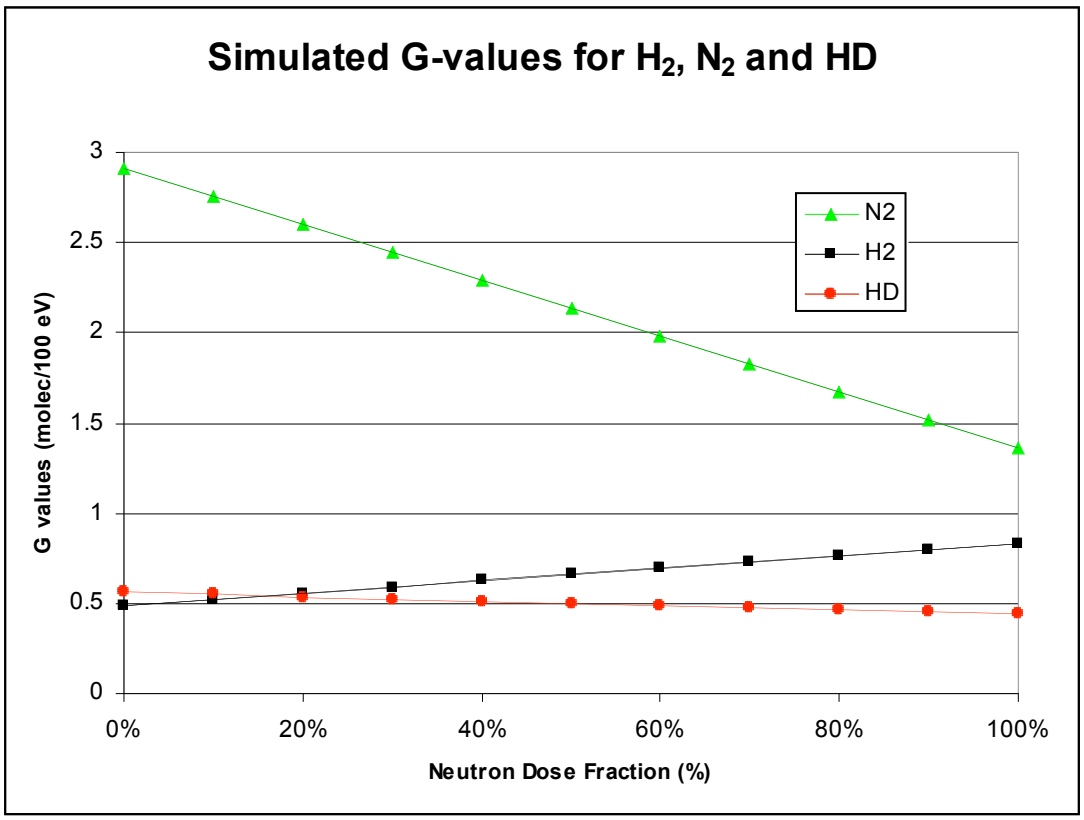

Figure 2.2-3 G-values for nitrogen, hydrogen and HD from simulation [10]

With a solution containing N_2O, the room temperature g-values, and neutron energy deposition, gamma energy deposition can be determined with the following steps:

1. Experimentally measure concentration of N_2 formed by radiolysis
2. Calculate concentration of N_2 formed by neutron radiolysis with 100% neutron g-value and neutron energy deposition
3. Subtract concentration of N_2 formed by neutron radiolysis to get N_2 formed by gamma radiolysis
4. Use gamma g-value to get gamma energy deposition

These steps, of course, can be carried out with H_2 or HD also. Values for neutron dose fraction can be calculated by dividing the neutron dose by the total absorbed dose.

Another method of calculating the neutron dose fraction is to divide the g-values of N_2 by H_2 (or HD), and fit that ratio to the neutron dose fraction. A chart of these ratios can be seen in figure 2.2-4. One of the problems with this method is the low slope of the ratios. If there is a small error in N_2/H_2, it results in a large error in neutron fraction. Because of the innate error in the ratio method, the subtraction method will be the technique of choice.

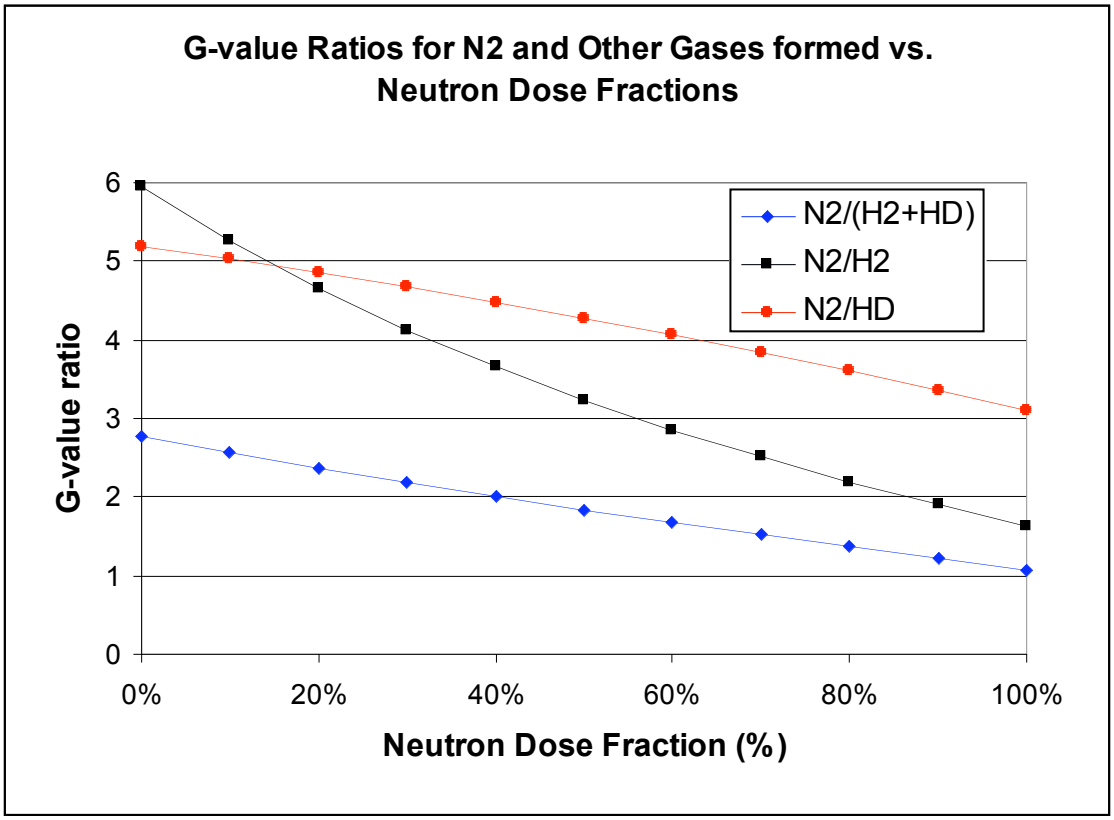

Figure 2.2-4 A chart of neutron energy fraction as a function of g-value ratios.

2.2.4 Scavenging Reactions

Scavenging reactions are used to detect radicals formed by radiolysis, just as in the gamma energy calibration. In order to detect radicals, scavengers must meet certain restrictions including the following: (1) they must quickly react with the radical, (2) they must be able to be dissolved in sufficient quantity, (3) they must be stable up to supercritical temperatures, (4) they must not interfere with other reactions of interest, and (5) they must produce a stable product that is measurable and only comes from the specific reaction of interest. All of these requirements are made to assure that all of the radical is consumed by the scavenger (not the surroundings) and

produces a measurable product. Scavenging reactions of interest to this project include the following:

$$N_2O + e^-_{aq} \rightarrow N_2 + O^- \quad \textbf{Eq. 2.2-1}$$

$$CD_3CD_2OD + H\bullet \rightarrow HD + (products) \quad \textbf{Eq. 2.2-2}$$

$$C_6H_5OH + H^\bullet \rightarrow (Non\text{-}interfering\ product) \quad \textbf{Eq. 2.2-3}$$

In Eq. 2.2-1, the nitrogen gas is measured in the mass spectrometer. It is important for the chemical reaction that all of the hydrogen radicals in the system are scavenged away by another reaction. Because of this, it was the original plan to combine the reactions of Eq. 2.2-1 and Eq. 2.2-2 in to the same experiment. At high temperatures however (above 200 C), the products formed in the reaction between ethanol-D6 (CD_3CD_2OD) and hydrogen radicals react with N_2O to create extremely high levels of nitrogen gas, interfering with the N_2 product formed in Eq. 2.2-1. Since the N_2O scavenging experiment cannot be run without hydrogen scavenging, other methods were attempted. First, cyclohexane ($CH_2(CH_2)_4CH_2$) was tested, but unrealistic yields of nitrogen gas were still seen. Finally, phenol (C_6H_5OH) was tested and was found to properly scavenge hydrogen radicals. Because of this, the reactions in Eq. 2.2-1 and Eq. 2.2-2 must be run separately at high temperature, whereas Eq. 2.2-1 and 2.2-3 will give aqueous electron data up to high temperature and Eq. 2.2-1 and 2.2-2 will give hydrogen radical data at high temperature and matching aqueous electron data below 200 C. The methods for each of the separate scavenging experiments are described in this section.

2.2.5 Aqueous Electron

The aqueous electron (e^-_{aq}) is detected via the reaction in Eq. 2.2-1. For this experiment, two water reservoirs are prepared: one is pH=7 filtered water saturated with N_2O, and the other a

pH=7 phenol solution saturated with helium gas (to sparge out other gases). The water flows are mixed at flow rates of 5% N_2O mixture and 95% phenol solution, with final concentrations of 0.0012 molar N_2O and 0.01 molar phenol. Typically, total flow rate is either 6 mL/min or 10 mL/min, and can be adjusted based upon desired energy deposition in the sample.

When the gaseous sample is analyzed, nitrogen (mass 28) and hydrogen (mass 2) levels are measured with the mass spectrometer. Other mass numbers of interest for this experiment include nitrous oxide (mass 44), water (mass 18) and mass 5, which acts as a zero for all experiments. If the nitrous oxide shows a peak in the time the region of interest for nitrogen, there will be an effect on the nitrogen signal. The same is true of water and hydrogen. As long as the GC column is working properly, the N_2O and H_2O will come out slow enough that they do not interfere with the other signals. If the GC column is not functioning, it may have to be baked out for a few hours before more data can be taken.

2.2.6 Hydrogen Radical

The hydrogen radical is measured in the same manner as the aqueous electron except that HD is the stable product being measured via the reaction in Eq. 2.2-1. In the case of mass 3, there is no interference with other gasses. The setup is also similar, two water reservoirs are prepared: one is pH=7 filtered water saturated with N_2O, and the other a pH=7 0.03 molar ethanol-D6 solution saturated with helium gas (to sparge out other gases). In this case, the N_2O is used to eliminate aqueous electrons from interfering with the alcohol, but N_2 yields are not measured because the alcohol interferes with the N_2O.

2.2.7 Neutron Energy Deposition Calibration

The neutron energy deposition experiment was performed with a 0.0100 molar solution of 99.95% +/- 0.05% purity sodium carbonate solution. The sample preparation included measuring 1.0600 g of sodium bicarbonate (mm=1.0599), and mixing it with 1L of water in a volumetric flask. The solution was run through the apparatus continuously for 25 minutes before the first data point was taken to reach steady state. Samples of approximately 10 mL were taken by timing collection time in 4 dram polyethylene vials. The actual sample size was recorded and used for calculation (not 10 mL). The pumping speed was calibrated prior to the experiment by measuring time to fill a 10 mL volumetric.

Samples were counted on two high purity germanium (HPGe) detectors. Count time was 300 seconds and the sample was positioned 3 cm away from the detector. Counting error at this position and count time was typically less than 1.0%, depending on the detector. The HPGe efficiency is calculated with a 10 mL liquid NIST standard europium source contained in a 4 dram vial, the same vials that are used for the sodium solution.

Three data points were taken over one day with the lead shield, while 22 data points were taken over two separate days with the lead shield removed. Activity was calculated using Eq. 2.2-4 (CR=count rate). The ratio of Na-24 to Na-23 atoms was then calculated and the MCNP calibration factor (CalFac) was used to calculate energy deposition as in Eq. 2.2-5

$$\alpha[Bq] = \frac{CR[c/s]}{\eta_{HPGe}} \times \exp(t\lambda) \qquad \textbf{Eq. 2.2-4}$$

$$E_{dep}[eV/g] = \frac{\alpha[Bq]}{\lambda} * CalFac\left[\frac{eV/g}{rxn/atom}\right] \qquad \textbf{Eq. 2.2-5}$$

The results of the activation analysis can be seen in table 2.2-1. The energy deposition with and without the lead shield from neutrons was calculated to be 3.23×10^{16} and 4.23×10^{16}

(100eV/g)*(mL/min) respectively. The total dose rate for a sample can be calculated from this number using the pump flow rate, density of the water in the irradiation volume, and total sample volume, as seen in Eq. 2.2-6. For a 10 mL sample at 46° C (density = 1 g/mL) pumped with a flow rate of 6 mL/min, the neutron dose would be 5.38×10^{15} and 7.05×10^{15} (100 eV/sample) with and without lead, creating 1.59×10^{-5} and 1.21×10^{-5} moles/L of nitrogen when using the data in figure 2.2-3.

$$E_{dep,sample}[100\ eV] = \frac{E_{dep}[\frac{100eV}{g} \times \frac{mL}{\min}]}{FlowRate[\frac{mL}{\min}]} \times \rho_{water,irradiation}[g/mL] \times Vol_{sample}[mL] \qquad \textbf{Eq. 2.2-6}$$

Lead Status	Ave. Activity (Bq/sample)	Count Error	Flow Rate	Samples Taken	MCNP Calibration Factor (100eV/g)/ (rxn/atom)	Energy Deposition (100 eV/g)*(mL/min)
Installed	9264.3	0.53%	9.950	3	5.38E+26	3.23E+16
Not Installed	19830.19	0.16%	6.009	22	5.53E+26	4.23E+16

Table 2.2-1: The results of the neutron activation analysis energy deposition calculation.

2.2.8 Gamma Energy Deposition Calibration

Following the neutron energy deposition calibration, a radiolysis experiment was performed to calculate the gamma energy deposition. In this experiment, nitrogen was formed by a reaction between aqueous electrons and nitrous oxide as in Eq. 2.2-1. From the data used to create the plot in **Figure** , the G-value for nitrogen formation via neutron irradiation is 1.36 molecules/100 eV. Combining this with the flow rate of the experiment (6.078 mL/min), the density of the water at 100 C (1.004 g/mL), the dose rates, and the data from Table 2.2-1, it is expected that a concentration of 1.20E-5 molar and 1.58E-5 molar will be generated with and without lead respectively. In the experiment, 4.95E-5 and 15.6E-5 moles/L were formed with and without the lead shield respectively, meaning that 3.76E-5 and 14.0E-5 moles/L of nitrogen

were created from gamma radiation. Again, the data from figure 2.2-4 can be used to determine the final gamma energy deposition. The results can be seen in Table 2.2-2 below.

	With Lead		Without Lead	
	Nitrogen	Hydrogen	Nitrogen	Hydrogen
Product Formed (Experimental Total) [molar]	4.96E-05	2.08E-05	1.56E-04	4.57E-05
Neutron Energy Deposition [100 eV/g]	5.31E+15	5.31E+15	6.96E+15	6.96E+15
Neutron G-value for Product [molecules/100 eV]	1.36	0.83	1.36	0.83
Expected Concentration Product from Neutrons (molar)	1.20E-05	7.35E-06	1.58E-05	9.63E-06
Concentration Product Formed from Gamma (molar)	3.76E-05	1.35E-05	1.40E-04	3.61E-05
Gamma G-value for Product [molecules/100 eV]	2.91	0.49	2.91	0.49
Calculated Gamma Energy Deposition [100eV/g]	7.74E+15	1.65E+16	2.89E+16	4.42E+16
Total Energy Deposition Neutron and Gamma [100eV/g]	1.31E+16	2.18E+16	3.59E+16	5.11E+16
Calculated Neutron Portion of Energy Deposition [%]	40.7%	24.4%	19.4%	13.6%

Table 2.2-2 The results of the gamma dose calibration.

The results of the nitrogen calibration of the gamma energy deposition give a total neutron contribution of total dose of 40.7% with lead and 19.4% without lead. Effectively, the lead shield has doubled the neutron contribution to total dose, but has also reduced total dose by a factor of approximately 3. Signals are thus smaller and noisier with the lead shield on, but are easier to separate the product formed by gamma from the neutron since the neutron contribution is larger. The hydrogen numbers match with the lead shield on, but not with the lead shield off. The nitrogen numbers are considered to be much better because the signals have less noise, are much larger, have a lower background (since H_2 is hard to pump from a vacuum chamber), and because the G-values are benchmarked on the simulation from proton radiolysis.

2.2.9 Scavenging Experiments

Following the energy deposition experiments, initial scavenging experiments were performed. The first experiment of interest was the nitrous oxide/phenol experiment. In this experiment, nitrogen formed by aqueous electrons as in Eq. 2.2-1 is measured along with hydrogen formation. The flow rate was approximately 6 mL/min, and was measured before each series of experiments. A background level of nitrogen was taken with the reactor off, and a 3 regime linear trend was found for nitrogen only (see figure 2.2-4). All other formed gases were at zero below 400 C. Since the low and intermediate temperature regimes have a fairly shallow slope, they are easy to use and subtract. Also, since the contribution is relatively small, the results can still be considered accurate even though the data fit is not good. Above 400 C, thermal decomposition dominates and far too much nitrogen is created with far too great a slope, making it impossible to get data at these temperatures.

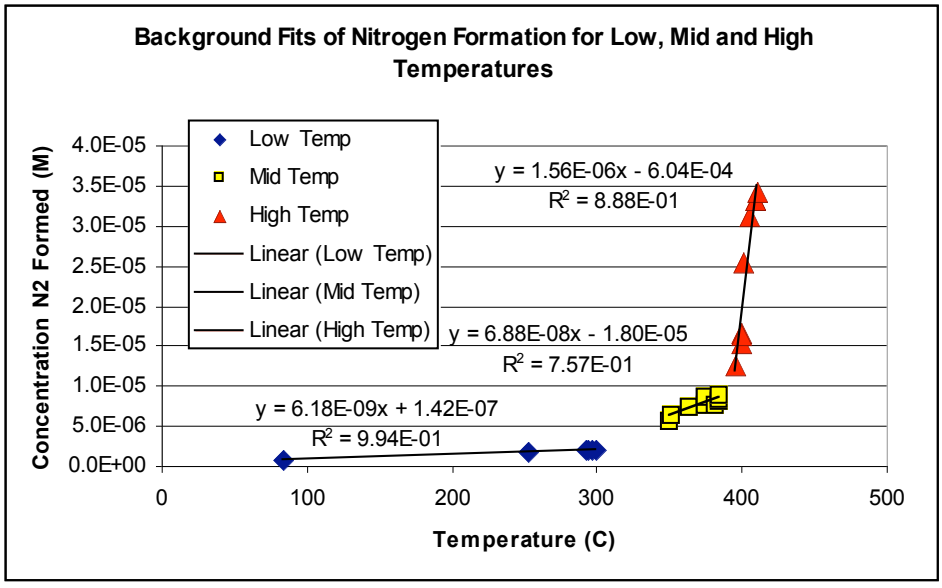

Figure 2.2-5: The background levels of nitrogen formed with the reactor off vs. temperature.

All current results are presented in the form of total G-value or molecules formed per 100 eV total energy, including both neutron and gamma energy. The preliminary results for nitrogen

can be seen below in figure2.2-7. From the results, it can be seen that more nitrogen is formed per unit energy with the lead shield off than on. This suggests that like the simulated G-values show, aqueous electrons are made in greater quantity by gamma energy deposition than neutron energy deposition. Above 400 C, it seems that this effect is reduced, as the product N_2 formed converges to approximately the same value.

Similar to the nitrogen results, the hydrogen results also follow the expected behavior according to the simulated G-values. In this case, more hydrogen gas is formed from neutron radiation than gamma radiation. The yield of hydrogen gets very high at higher temperatures and it is unclear, at this point, whether this is a real effect, or if there is some thermal breakdown of the water.

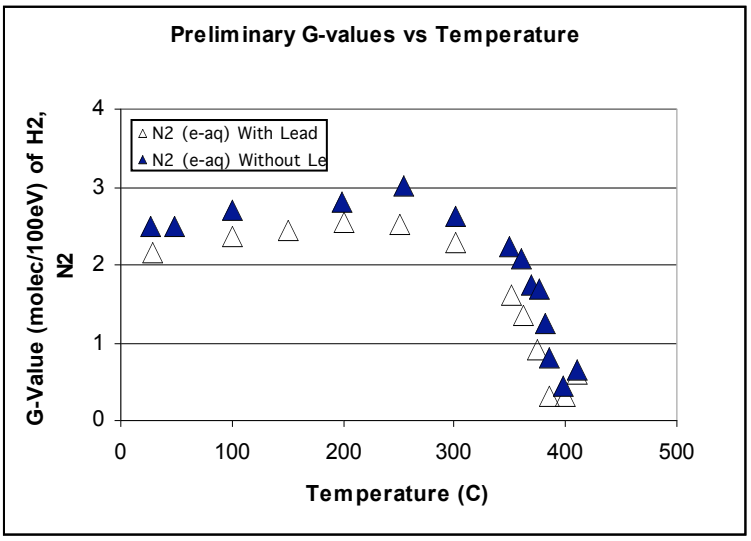

Figure 2.2-6: The nitrogen results with and without the lead shield installed. The G-values are for total energy deposition, neutron plus gamma.

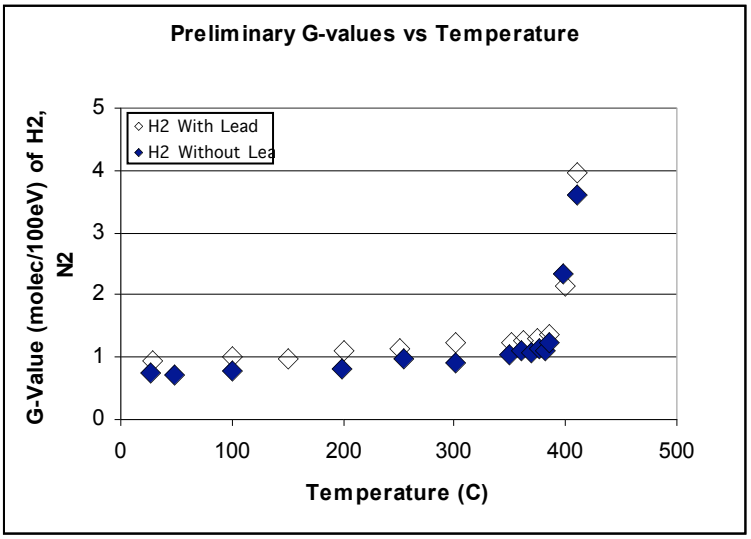

Figure 2.2-7 The hydrogen results with and without the lead shield installed. The G-values are again for total energy deposition, neutron plus gamma.

In addition to the phenol/N_2O tests, initial ethanol-D6/N_2O tests have been performed. In this experiment, nitrogen production mirrors the nitrogen produced in the preceding experiment up to 150 C, and then it increases due to the interference of products formed from ethanol. This effect creates G-values up to 25 molecules/100 eV, which would mean many more aqueous electrons were formed than water molecules could have possibly been broken, since the bond energy is higher than 4eV. The hydrogen radical yield, measured with HD, showed similar behavior to the H_2 results, except that the HD production seems to begin to increase at a much lower temperature than H_2. There is evidence that the hydrogen radical production goes down at 400 C, but repeated experiments will be necessary to determine whether the effect is real, or if there was a problem with the chemistry on the inlet water (such as a lack of ethanol D6).

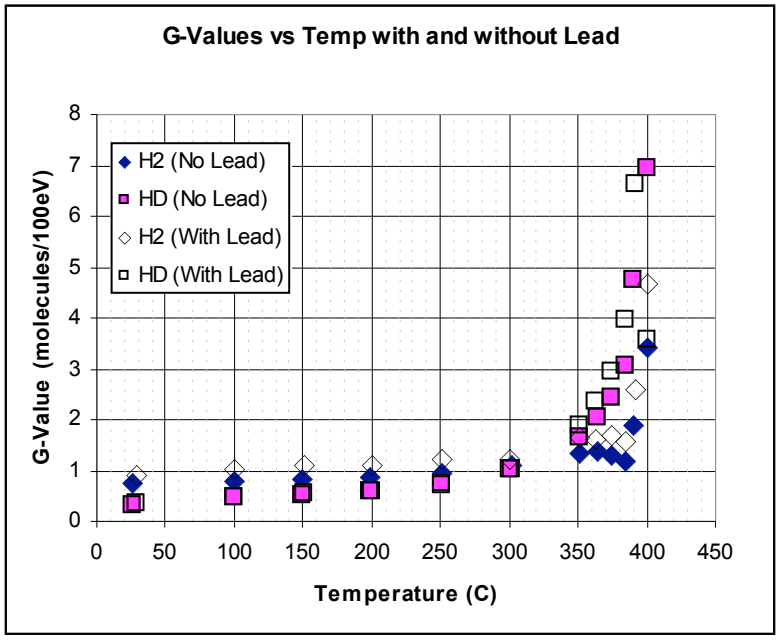

Figure 2.2-8 The results of the ethanol-D6 and N_2O testing.

3. Reaction Rate Results

For a full model of the radiation chemistry including the effects of added scavengers, one requires rate constants for recombination of the free radicals $(e^-)_{aq}$, OH, and H atom [1,11]. For these three primary radicals there are six recombination rate constants. These second order rates are very difficult to measure properly, because in general the time-dependent kinetics data gives a parameter like k/ε , which combines the desired rate constant k with a concentration scaling factor like the molar extinction coefficient ε. Somehow a way must be found to determine the absolute concentration of the transient. This is what makes second order kinetics so much more difficult than first order [12].

As a first step we have been trying to measure the six second order rate constants up to 350°C using standard pulse radiolysis/transient optical absorption on a microsecond timescale.

For solvated electrons, the absorbance is very strong, and one can assume based on the properties of the spectrum that its intensity is not a strong function of temperature. We have been able to determine rate constants for H + $(e-)_{aq}$ and $(e-)_{aq}$ + $(e-)_{aq}$ as described below. The rate constant for OH + OH has recently also been determined after a large amount of work to determine its extinction coefficient vs. temperature. As part of that effort, we measured the rate constant for H + O_2 and H + HO_2 . This has given us new insights which should allow us to estimate the rate for H + OH radical from *ab initio* calculations. The remaining recombination for OH + $(e-)_{aq}$ should now be possible to extract from kinetics data which is presently being collected.

3.1 H+$(e-)_{aq}$ and $(e-)_{aq}$ + $(e-)_{aq}$

A very extensive set of data was collected for the system of alkaline water with high pressure of added H_2. In hydrogenated alkaline water and small radiation doses, the transient absorption from $(e^-)_{aq}$ can be approximated by just three dominant reactions:

$$H_2 + OH^\bullet \rightarrow H^\bullet + H_2O \qquad (1)$$

$$H^\bullet + OH^- \Leftrightarrow (e^-)_{aq} + H_2O \qquad (2)$$

$$e^-_{aq} + e^-_{aq} \rightarrow 2\ OH^- + H_2 \qquad (3)$$

Reactions (1) and (2) occur with pseudo-first-order kinetics at nanosecond and microsecond times respectively depending on the actual concentrations of H_2 and OH- used. The subsequent recombination is then purely second order via equation (3). At higher dose and lower OH- concentration, the concentration of H atoms may become very substantial for a microsecond or two. In this situation the cross recombination (4)

$$H + e^-_{aq} \rightarrow OH^- + H_2 \qquad (4)$$

briefly becomes the dominant decay reaction. This is illustrated by the data shown in figure 3.1A. Four kinetic traces corresponding to four different electron pulse widths (4-40ns) are shown on both long (panel a) and short (panel b) timescales. As the dose increases, the signal decays very quickly within a short time. At longer times the decays become almost identical as expected for pure second-order decay.

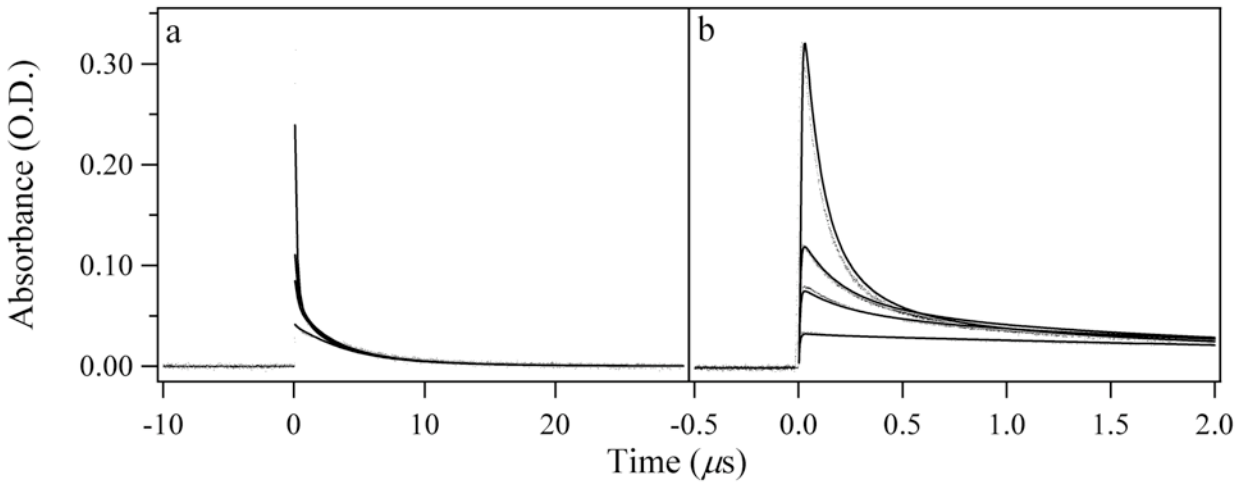

Figure 3.1A. Transient absorption of e^-_{aq} at 1050 nm (points) as acquired over a wide range of doses, and global fits to the kinetics (solid lines). Temperature = 250 °C, OH^- concentration = 1.0×10^{-4} m, pressure = 250 bar.

The behavior of bimolecular recombination reaction (3) is shown in the Arrhenius plot 3.1B. The temperature dependence is as strange as the reaction itself. It is purely diffusion limited from room temperature up to 150°C. Then the reaction abruptly "turns off", and by 250°C it is actually slower than at room temperature. It became too slow for us to measure above 250°C. The reaction is almost certainly unimportant in water at supercritical temperatures.

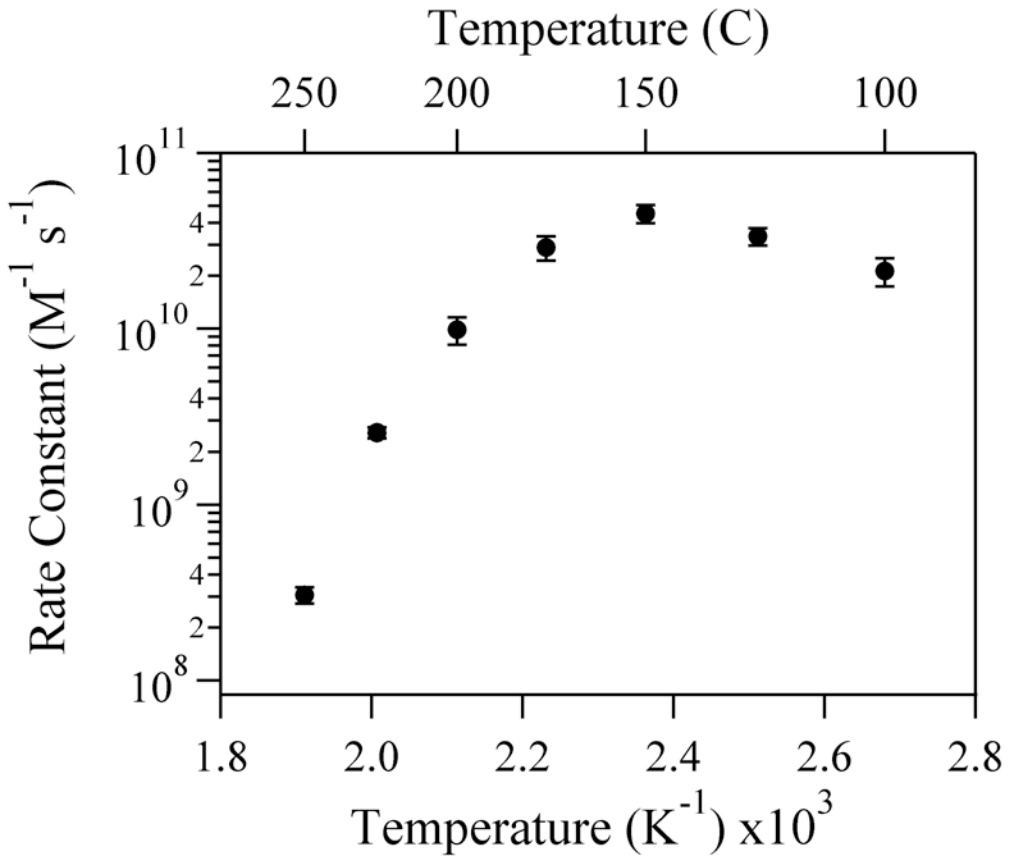

Figure 3.1B. Arrhenius plot for bimolecular recombination of hydrated electrons.

The same chemical system allowed us to measure the cross reaction (4) from the very fast decay at short time, illustrated in figure 3.1A. The Arrhenius plot is shown in figure 3.1C. This reaction is very fast at room temperature, and just keeps becoming faster at higher temperature. It is almost certainly important as a recombination pathway in supercritical water.

We should note that this evaluation of both reactions (3) and (4) at elevated temperature very significantly modify previous attempts to extrapolate lower temperature data to PWR conditions.

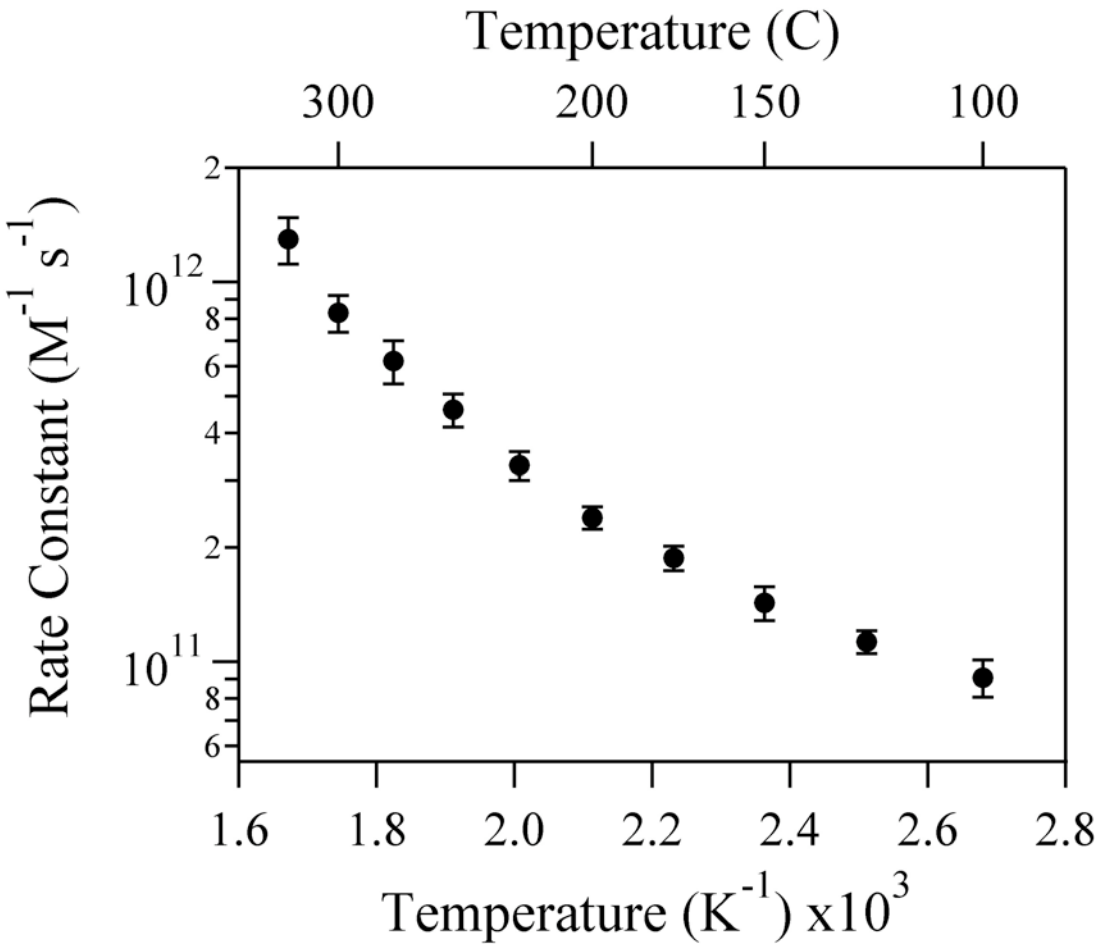

Figure 3.1C. Arrhenius plot for reaction of H atoms with hydrated electrons.

3.2 OH + OH

The experiments to measure bimolecular recombination of OH radicals were

$$OH + OH \rightarrow H_2O_2 \qquad (5)$$

extremely difficult because the weak absorption of OH is deep in the ultraviolet where probe light is also weak. In addition the sapphire windows of the cell produced a transient absorption of similar magnitude to the transient of interest. Finally, the absorption coefficient of OH radical was found to decrease as the temperature increased, making the experiment more and more

difficult. And it forced us to do all the work to measure the absorption coefficient. Details of all this work are in the paper submitted to Journal of Physical Chemistry. For our purposes here we just display the result in figure 3.2A.

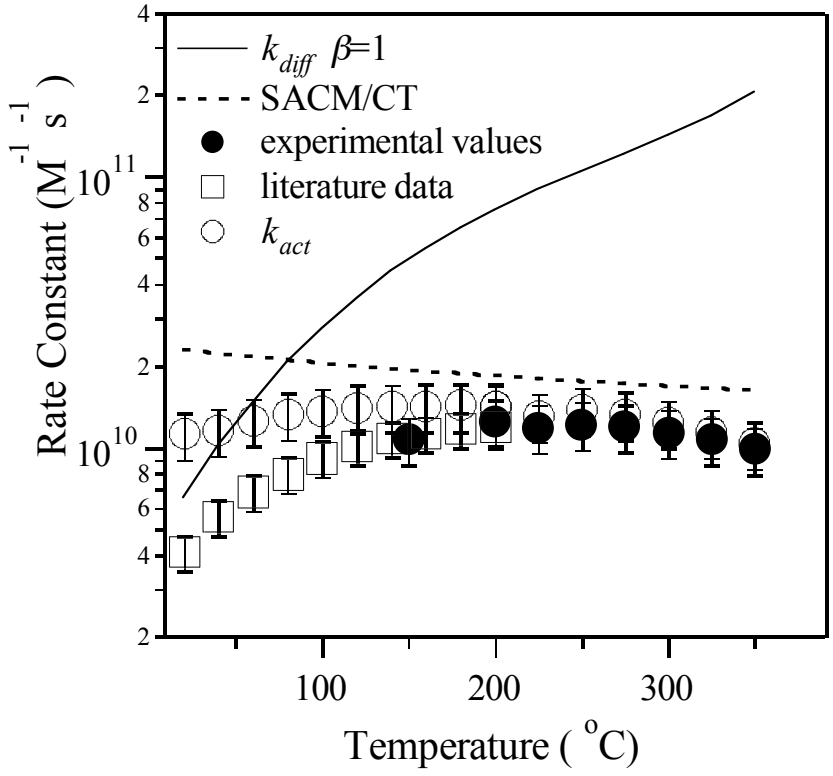

Figure 3.2A. Rate constants for bimolecular recombination OH + OH → H_2O_2.

Figure 3.2A displays the present results (black circles) together with literature data for lower temperature (open squares). We have excellent agreement with the previous results in the region of overlap. The most obvious observation is that the rate constant barely changes above 150°C, staying at a value around 1 x 10^{10} M^{-1} s^{-1}. Previous attempts to extrapolate to 350°C would give an answer 2-3 times higher.

We have used the Noyes equation $k_{obs}^{-1} = k_{act}^{-1} + k_{diff}^{-1}$ to decompose the observed rate constant into the diffusion-limited rate and the "activated barrier" rate. Our estimate of the diffusion limit for this reaction is based on the Smoluchowski equation and is plotted as a solid

line on figure 3.2A. From this estimate and the observed rate constants, we infer the values of k_{act} as shown by the open circles on figure 3.2A. As might be expected from the behavior, the reaction is nearly diffusion limited at room temperature, but above 200^{o}C is almost entirely limited by some barrier.

The dashed line on figure 3.2A represents the gas phase high pressure limit for the same reaction calculated by a high level ab initio SACM/CT method. Clearly this high pressure limit rate is in excellent agreement with the observed liquid phase result. The effective barrier to reaction is essentially entropic, as a certain angular orientation of the pair of OH radicals is required for the (barrierless) reaction channel. The surprise is that hydrogen bonding of OH to the water seems to make so little difference in this system. Water seems to act mainly as a very efficient third body for the recombination. This leads us to conclude that we probably can use *ab initio* calculations to accurately estimate the rate for the cross reaction (6),

$$OH + H \rightarrow H_2O \qquad (6)$$

which is very difficult to measure.

3.3 H +O_2 and H + HO_2

In the reaction system for measuring OH + OH, the HO_2 radical is also formed as a minor secondary product, but it appeared that its absorbance was important. So we measured this absorbance by generating the HO_2 radical via reaction (7) in H_2 saturated water.

$$H + O_2 \rightarrow HO_2 \qquad (7)$$

This provided the opportunity to also measure directly the reaction rate for this reaction from the product growth.

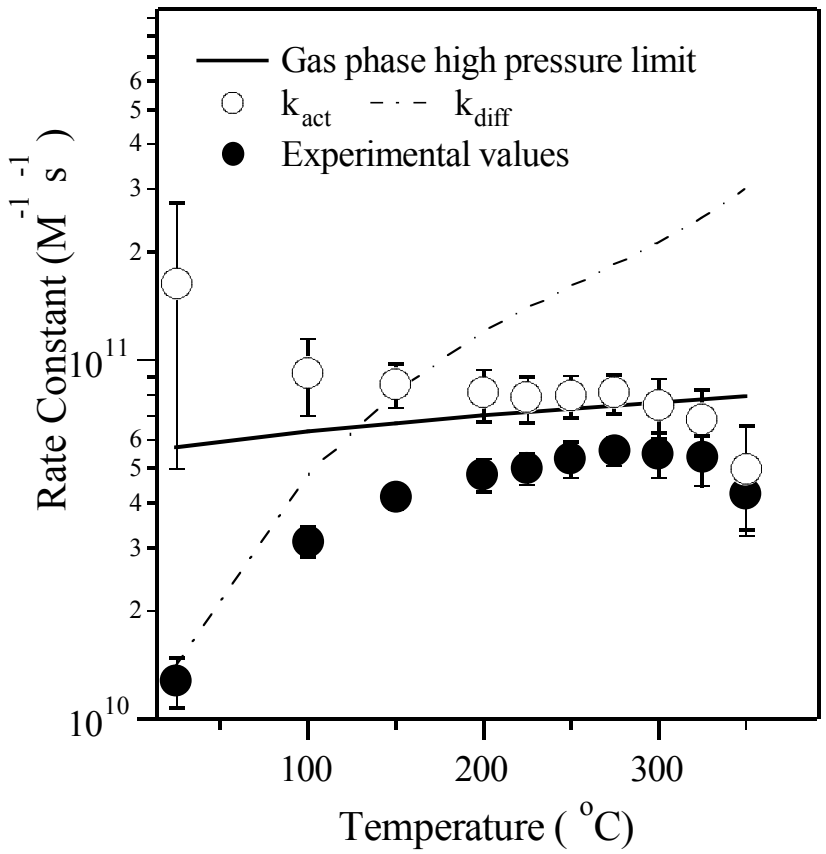

Figure 3.3A. Reaction rates for H + O_2.

The experimental reaction rates for reaction (7) are plotted in figure 3.3A as the solid circles. Much like the result for OH + OH shown above, there is little change in the rate constant above 200^{o}C. Just as for the previous reaction we can estimate the diffusion limit (dashed line), and extract the "activated barrier" reaction rate as the open circles. At room temperature the reaction is almost entirely diffusion limited. At 350^{o}C the reaction is entirely limited by a barrier. The solid line is the gas phase high pressure limit for this reaction. The aqueous phase reaction and the gas phase rate are in virtually perfect agreement. The barrier, once again, is entropic, as only for an approach of the H atom at about 45 degrees with respect to the O-O axis is there no potential energy barrier. There must be many re-encounters due to the cage effect, in

order for the reaction to be diffusion limited. At high temperatures diffusion becomes too fast, and the cage effect is too weak, for the diffusion limit to prevail.

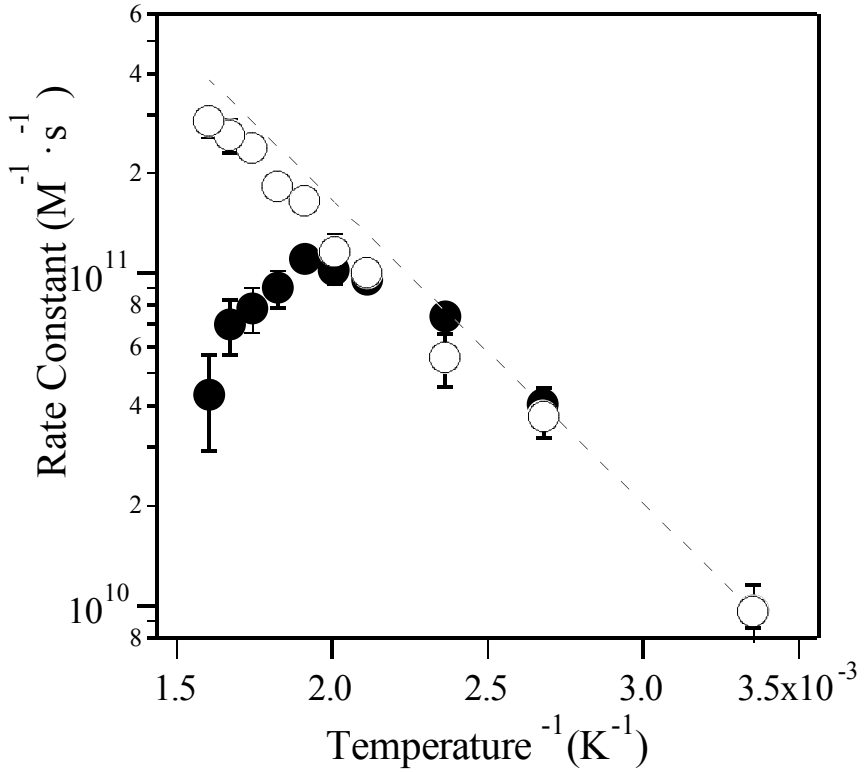

Figure 3.3B. Reaction rates for the reaction H + HO_2 . Filled circles represent formation of H_2O_2, while open circles represent the alternative formation of 2 OH radicals.

An important cross-reaction encountered in this system at high temperature was reaction of H with the product radical HO_2. In all previous studies of this reaction in water (up to 150°C) it has been asserted that the product is H_2O_2, as

$$H + HO_2 \rightarrow H_2O_2 \qquad (8a)$$

If this is correct then we should see a strong decrease in our product absorbance from HO_2 at temperatures above 200°C. The product absorbance does not decrease, and so in order to fit our data we were forced to postulate that the reaction rate (8a) decreases, as indicated by the solid

circles in the Arrhenius plot 3.3B. However, further investigation of the gas phase mechanisms indicates that the preferred mechanism occurs on a triplet surface as

$$H + HO_2 \rightarrow OH + OH \qquad (8b)$$

This mechanism is perfectly compatible with our data and suggests the near-Arrhenius behavior shown by the open circles in figure 3.3B. Assuming this is correct, it could have significant impact in the chemistry determining critical hydrogen concentration in reactors.

4. Critical Hydrogen Concentration

The addition of a small overpressure of hydrogen to reactor cooling loops is the basis for "hydrogen water chemistry", a spectacularly successful strategy for slowing stress corrosion cracking in the steel of water cooled reactors. Part of the effect is due to suppression of peroxide in the bulk water radiolysis. The critical reaction is $H_2 + OH \rightarrow H + H_2O$, which converts the oxidizing OH radical into the reducing H atom. The H atoms can then reduce H_2O_2 and O_2 formed in spur chemistry back to water. The H_2 concentration coming out of the core is the same as the concentration going in, thanks to this dynamic equilibrium. The minimum H_2 concentration required to pull off this kinetic trick is called the "critical hydrogen concentration", which does depend on dose rate, neutron/gamma ratio, and temperature, so the integrated quantity measured in reactors depends on the reactor design.

The basic question we asked is, will this chemistry also work in a supercritical water cooled reactor? We still lack much basic information needed to model the chemistry in supercritical water. But it should be straightforward to answer the question using the apparatus described in sections I and II above. We simply apply some radiation dose to pure water, and

look for the effect of added hydrogen on the oxygen and hydrogen exiting the radiation zone for different temperatures and pressures.

The first difficulty we encountered is that hydrogen peroxide generated in the radiolysis does not quantitatively decompose on the hot metal tubing according to the expected stoichiometry

$$2\ H_2O_2 \rightarrow\ O_2 + 2\ H_2O$$

Significantly more H_2 exits the system than O_2. We presume this is due to corrosion reactions on the tubing walls.

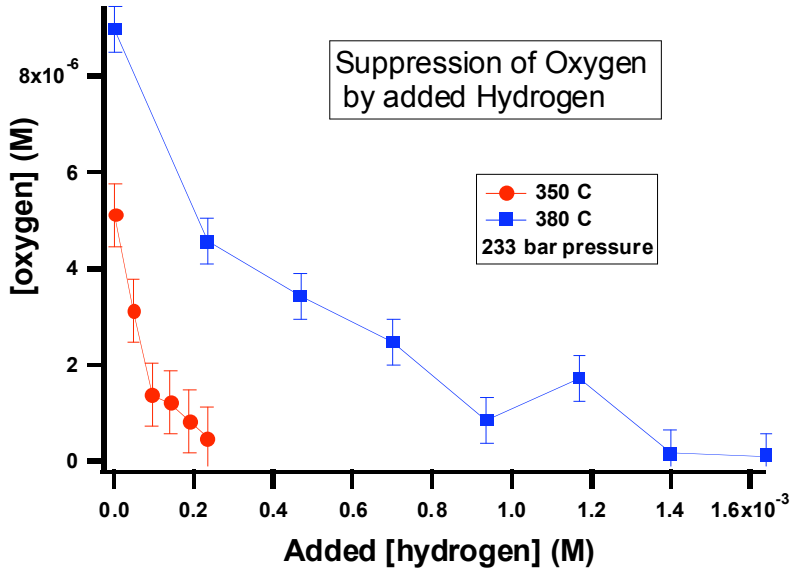

Figure 4A. Suppression of oxygen formation by added hydrogen for both subcritical and supercritical water.

In the beta radiolysis experiment, a usable oxygen signal does appear above 300°C. In figure 4A we plot the oxygen exiting the irradiation zone, as a function of the added hydrogen for both subcritical water (350°C) and supercritical water (380°C). In both cases we are able to suppress oxygen by added hydrogen. An important result is that it takes significantly more H_2 added in the supercritical water case. However, one should realize that the density of the water

in the two experimental conditions differs by a factor of three, and therefore the actual molar concentration of hydrogen in the radiation zone also differs by a factor of three. If one normalizes for this difference, the behavior in subcritical and supercritical water is not very different for these two particular temperatures and pressures.

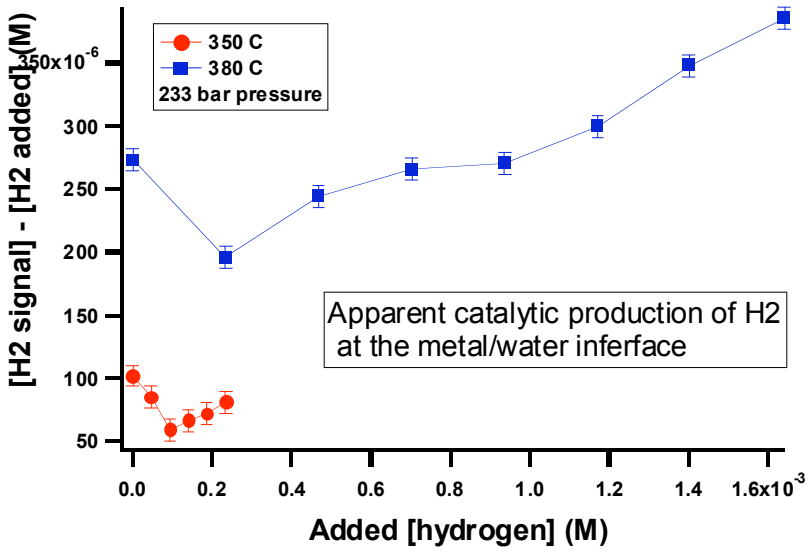

Figure 4B. Radiolytically generated hydrogen as a function of added hydrogen.

A complementary way to look at the suppression of water radiolysis by added hydrogen is to compare the hydrogen coming out vs. the hydrogen going into the radiation zone. Ideally, at the critical hydrogen concentration or higher, these quantities will be equal, and their difference will go to zero. In figure IVB we plot the observed hydrogen out-hydrogen in for the same experimental conditions. At low hydrogen in, we see a decrease in hydrogen out as expected. However, we then see an increase in the hydrogen coming out at higher added hydrogen. We do not at present understand this behavior, and work is continuing. Possibly the radiation is stimulating production of H_2 at the water/metal interface, and this is affected by the presence of added hydrogen at the surface. If this is the case it could be a very important effect

in reactors because it would change the average H_2 concentration at the surface. It might not be noticed in a much larger flow system where the surface/volume ratio is much smaller.

5. Corrosion Evaluation in SCW

A detailed evaluation of corrosion performance of a number of candidate code-certified and experimental alloys in has been performed in SCW environment at temperatures ranging from 370°C to 600°C for exposure durations of up to 1000 hours. Most studies were performed at an oxygen content of 25ppb (slightly above the targeted operating condition of SCWR), but test was performed at 2000ppb oxygen content to simulate a scenario that may occur during radiolysis of SCW. Two innovative approaches are also being investigated to enhance the performance of the candidate code-certified alloys: (i) grain boundary engineering and (ii) surface engineering.

5.1 Alloys Evaluated for Corrosion:

Four classes of materials are being examined for use in various components of SCWR: ferritic steels containing 2 to 12% Cr, austenitic steels, Fe-Ni based superalloys, and zirconium-alloys. Table 4.1A provides a sampling of alloys that are being tested in the University of Wisconsin supercritical water research program. The alloys listed have been selected based on their code-certification status and prior service in nuclear reactors or fossil boilers. Only results of select alloys are presented in this paper.

Table 4.1A. Nominal Compositions of Alloys being Investigated in the University of Wisconsin SCW Research Program.																		
Alloy	**C**	N	**Al**	**Si**	**P**	**S**	**Ti**	**V**	**Cr**	**Mn**	**Fe**	**Co**	**Ni**	**Cu**	**Nb**	**Mo**	**Ta**	**W**
Ferritic																		
HCM12A	.11	.063	.001	.27	.016	.002	-	.19	10.83	.64	Bal.	-	.39	1.02	.054	.3	-	1.89
T91	.1	.048	.022	.28	.009	.003	-	.216	8.37	.45	Bal.	-	.21	.17	.076	.9	-	-
HT-9	.21	.005	<.01	.30	.013	.005	<.01	.3	11.94	.69	84.36	.03	.62	.02	-	1.03	-	.48
NF616	.109	-	.005	.102	.012	.003		.194	8.82	.45	Bal.	-	.174	-	.064	.468	-	1.87
9Cr ODS*	.14	-	-	.048	<.05	.003	.21	-	8.6	.05	Bal.	-	.06	-	-	-	-	2
Austenitic																		
800H	.069	-	.5	.13	.014	.001	.57	-	2.42	.76	45.26	-	31.59	.42	-	-	-	-
D9	.039	.004	<.01	.8	.005	.003	.34	.01	13.7	2.03	Bal.	<.01	15.8	<.01	-	1.65	<.01	-
SS316	.017	.053	<.01	.55	.025	.002	<.01	.06	17.29	.91	Bal.	.11	10.9	.24	-	2	-	-
347	.08	-	-	1.0	.045	.03	-	-	17-19	2.0	Bal.	-	9-13	-		-		-
Fe-Ni based																		
625	.01	-	.2	.11	-	.001	.21	.014	21.9	.08	4.39	.05	61.22	.19	-	8.43	.004	-
718	.031	-	.57	.1	-	.001	1.05	.017	18.11	.08	18.04	.04	53.85	.03	5.03	2.96	.008	.015
690	.032	-	.2	.03	-	.0007	.35	.013	29.58	.2	1.23	.009	59.32	.008	<.001	.011	.001	.002
Zr-alloys																		
Zr-1.32%Sn-0.18%Fe																		

Y_2O_3: 0.33 wt.%

4.2 Ferritic Steels

After exposure to supercritical water all ferritic steels exhibited a build-up of an oxide layer on the surface, the thickness of which depended on the exposure time, temperature, and steel composition. Typical surface morphology of the oxide layers developed on ferritic steels is shown SEM plan view in Figure 5.2A for steels, NF616 and T91. The surface of the oxide layer showed discrete oxide grains of polyhedral morphology, 1 to 10mm in size. In some steels the oxide grains themselves exhibited pits, the origins of which are presently being investigated. There was no evidence of oxide erosion or its delamination from the underlying steel substrate.

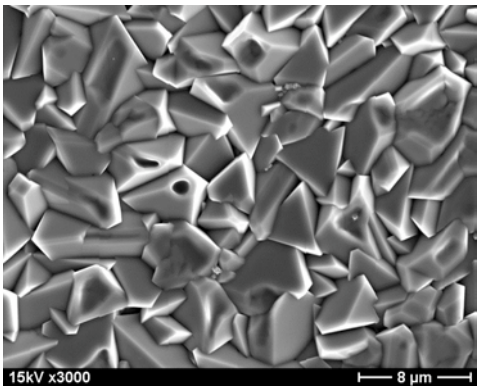

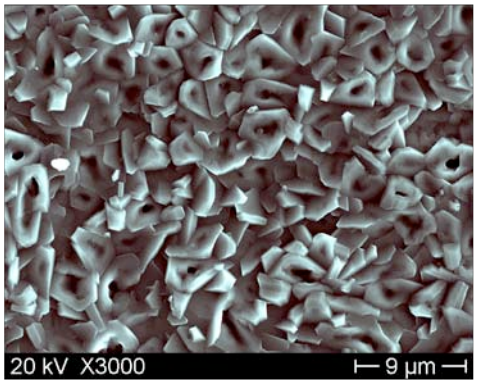

(a) (b)

Figure 5.2A. SEM plan view showing the surface morphology of the oxide layers formed on ferritic steels after exposure for 500 hours in SCW at 500°C with 25ppb oxygen concentration (a) NF616 steel and (b) T91 steel.

SEM cross-sectional examination of the oxide layers showed that in all ferritic steels, the oxidized region consisted of three distinct layers: a porous outer Fe3O4 magnetite layer, a inner dense Fe-Cr oxide spinel layer, and an internal oxidation layer. Figure 5.2B shows the cross-sectional view of this oxide layer for ferritic steel HCM12A along with the corresponding EDS elemental line scan across the oxide layer. The interface between the spinel and the magnetite layers represent the original surface of the alloy.

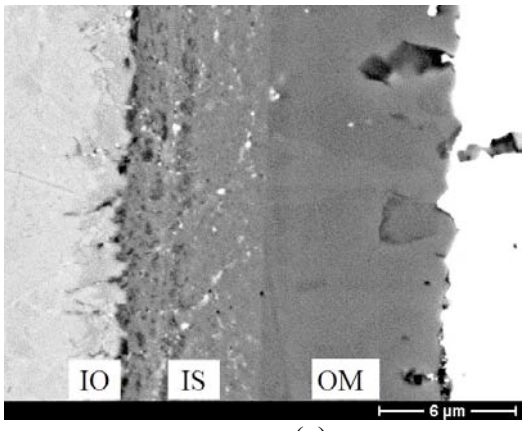

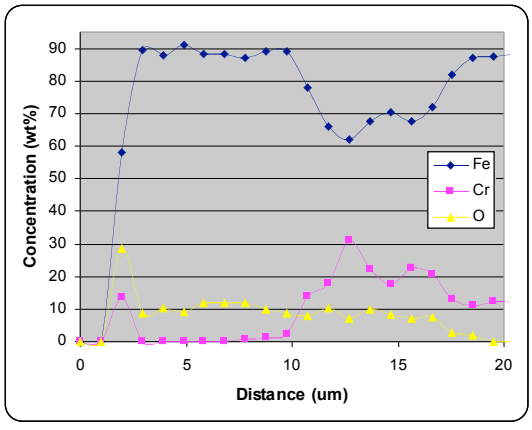

(a) (b)

Figure 5.2B. (a) SEM cross-sectional view showing the oxide thickness and morphology for ferritic steel HCM12A after exposure for 500 hours in SCW at 500°C with 25ppb oxygen

concentration showing the outer magnetite [OM], inner spinel [IS], and internal oxidation [IO] layers (b) corresponding SEM-EDS analysis across the oxide layer.

Weight gain measurements (DW) for ferritic steels after exposure to SCW for various durations (t), were plotted according to generalized equation, $DW=kt^n$ (k and n being constants), as shown in Figure 5.2C for ferritic steels, NF616, HCM12A, and 9Cr-ODS steel. Although a limited data set was used, the trends in growth rate were indicative of parabolic growth behavior, with the value of the exponent 'n' ranging from 0.4 to 0.6, in most cases. In general, the Cr-content of the steel was noted to be a strong determinant of the corrosion performance with a consistently lower weight gain observed for 12%Cr ferritic steels compared to the 9%Cr ferritic steels. A notable exception was the 9% Cr containing oxide dispersion strengthened (ODS) ferritic steel, which showed a lower weight gain compared to the 12%Cr steels. However there are other notable differences in the ODS steel such as the presence of small amounts of yttrium oxide dispersions and its substantially finer grain size and method of fabrication.

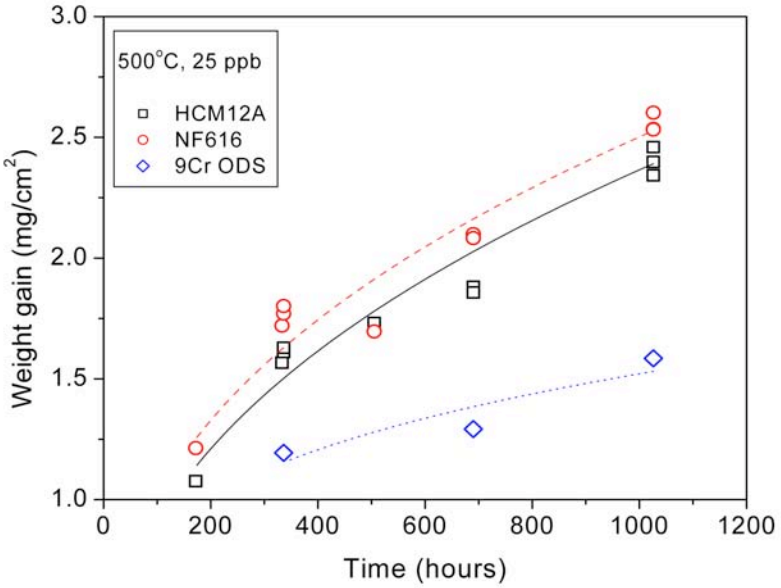

Figure 5.2C. Weight gain measurements for HCM12A, NF616, and 9Cr-ODS ferritic steels after exposure in SCW at 500°C with 25ppb oxygen for various durations.

5.3 Austenitic Steels

Austenitic steels exhibited a significantly lower oxidation compared to the ferritic steels as measured by weight gain after high temperature exposures in SCW. For example, Figure 5.3A shows the weight gain for austenitic steel D9 in comparison with the ferritic steel HCM12A. However, the weight gain measurements were less predictable for austenitic steel due to propensity for oxide spallation. Evidence of spallation was manifested as irregularities in the thickness of the oxide scale in SEM cross-sectional images, as shown in Figure 5.3B(a) for D9 austenitic steel. As in the case of the ferritic steels the outer oxide layer in austenitic steels consisted of Fe3O4 magnetite, and the inner layer consisted of (Fe, Cr) oxide spinel phase. However, in between the spinel layer and the base steel a Ni-enriched oxide layer is observed owing to the presence of Ni in these alloys (Figure 5.3B(b)).

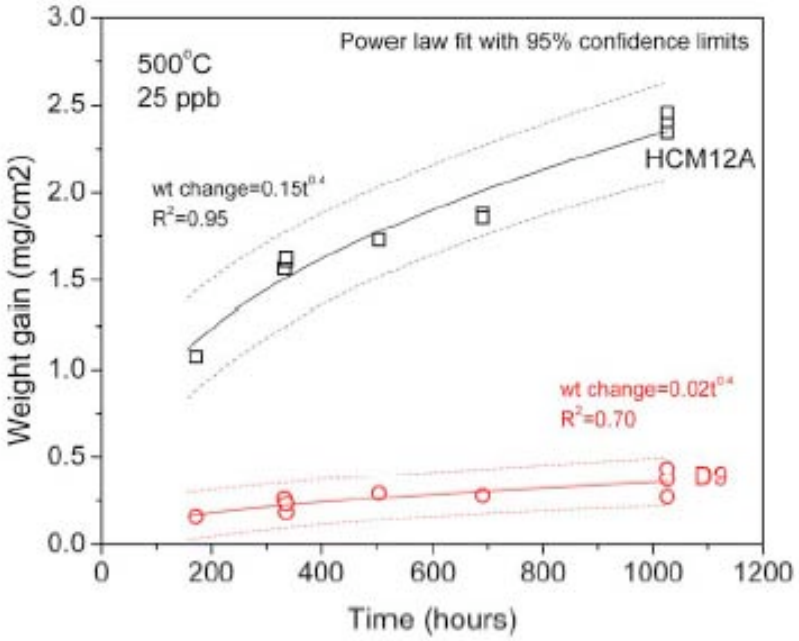

Figure 5.3B. Weight gain of austenitic steel D9 after exposure in SCW at 500°C with 25ppb oxygen for various durations. For comparison weight gain for ferritic steel HCM12A exposed to similar conditions is also shown.

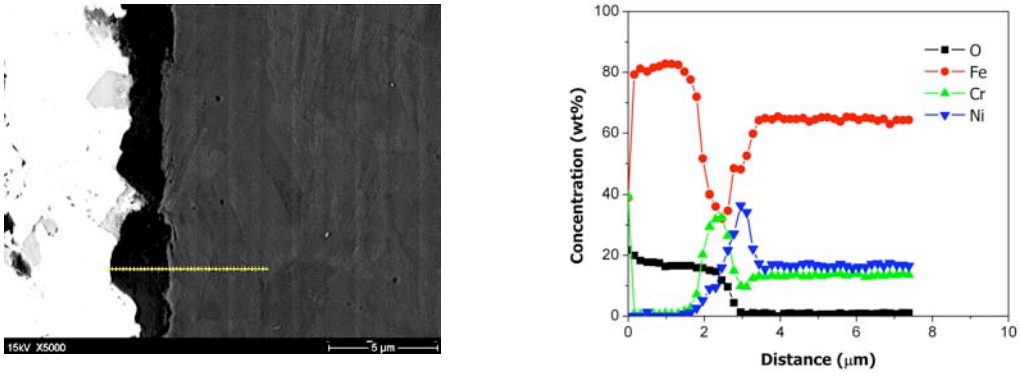

Figure 5.3B. (a) SEM cross-sectional image showing the oxide thickness for austenitic steel D9 after exposure in SCW at 500°C with 25ppb oxygen for 690 hours and (b) corresponding SEM-EDS analysis across the oxide layer.

Figure 5.3C summarizes the weight gain due to oxidation of various steels after exposure to SCW at 600°C for 6 weeks. For the ferritic steels, the 9% Cr steels as a class exhibited a higher weight gain compared to the 12%Cr steels. A notable exception was the 9%Cr ODS steel which exhibits a lower corrosion than either the 9% or 12%Cr steels. This is attributable to the finer grain sizes of these steels and the presence of Y2O3 dispersions in these steels, particularly at the grain boundaries where there inhibit the diffusion of oxygen.

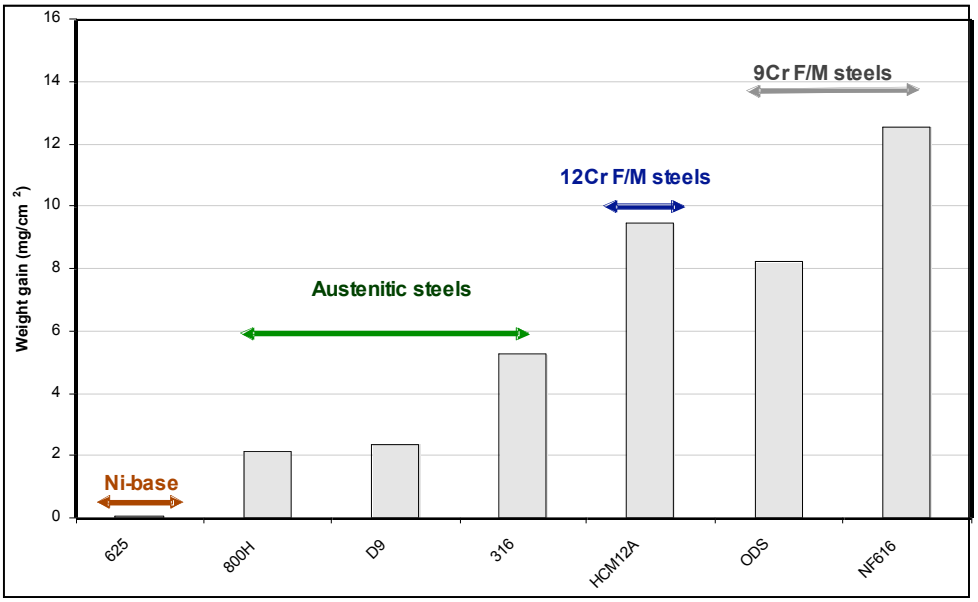

Figure 5.3C. Weight gain due to corrosion of various alloys after exposure to SCW at 600°C for 6 weeks.

5.4 Effect of Oxygen Content SCW Environment

As expected, increasing the oxygen content of the SCW from 25ppb to 2000ppb increased the weight gain due to oxidation, as shown for ferritic steel HCM12A in Fig. 5.4A. However, there was a distinct difference in the structure and morphology of the oxide scale that formed in the higher oxygen content SCW environments, as shown in Figure 5.4B for T91 ferritic steel. The oxide grains formed in the 2000ppb oxygen content environment were finer and had more interconnected porosity compared to those formed in 25 ppb oxygen content environment, making it more amenable to oxygen and ion diffusion. The phase distribution across the oxide layer for samples exposed to higher oxygen SCW environment indicated that the oxide scale is composed of three different layers: a porous outer hematite layer, underneath which is a relatively dense magnetite layer followed by a predominantly spinel iron/chromium oxide layer closest to the base steel.

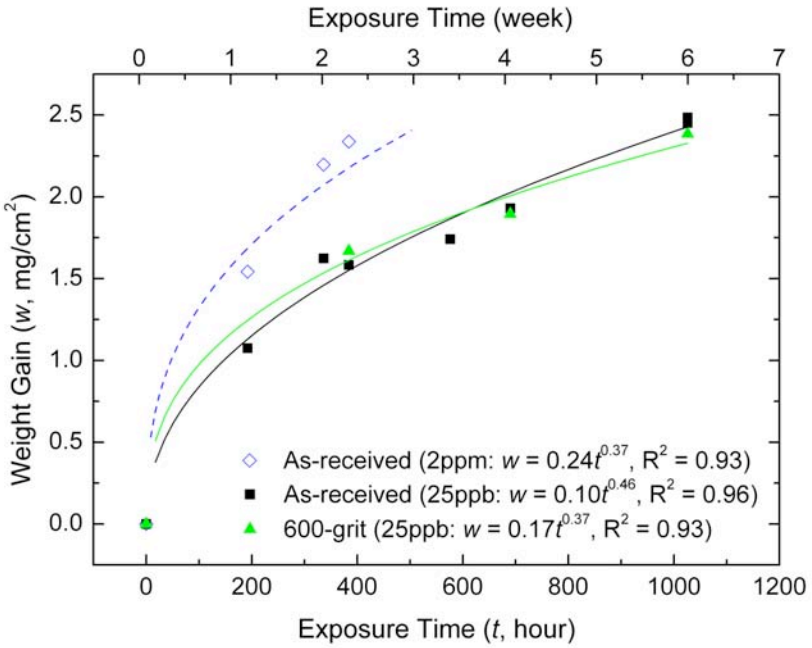

Figure 5.4A. Weight gain of ferritic steel HCM12A as a function of exposure time in SCW at 500°C with 25ppb oxygen and 2000 ppb dissolved oxygen concentrations.

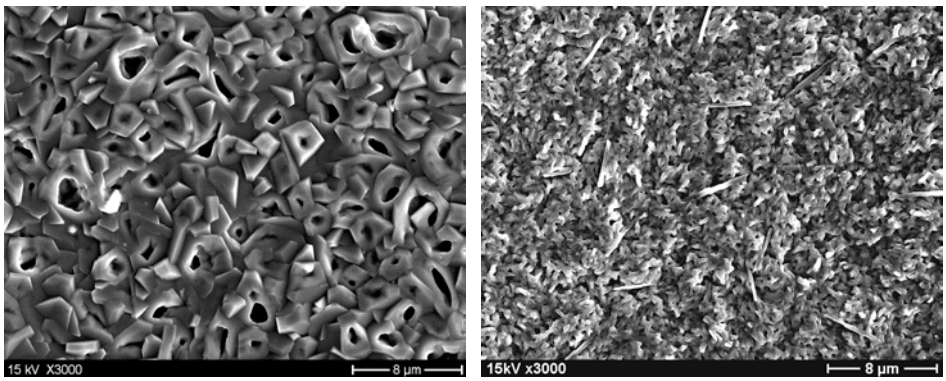

(a) (b)

Figure 5.4B. SEM plan view of the surface oxide formed on T91 after exposure for 500 hours in SCW at 500°C with (a) 25 ppb oxygen dissolved concentration and (b) 2000 ppb dissolved oxygen concentration.

5.5 Surface Modification Studies:

Surface modification of these candidate code-certified alloys was noted to have an effect of the total oxide thickness, oxide growth kinetics, and the morphology of the oxide layer. Oxygen ion implantation of the steels led to a lower oxide thickness and growth rate when exposed to SCW at 500ºC for up to 3 weeks. It was demonstrated by electron microscopy (and confirmed by XPS) that the oxygen ion implantation results in a fine (~ 10nm) distribution of spherical oxide precipitates in the near-surface regions of the steels. It is speculated that these oxide particles, increase the nucleation and particulate density of the thermal oxide that forms during initial stages of exposure to SCW, thereby making it more impervious during later stages of growth. X-ray diffraction of the oxidized surface also showed that the texture of the oxide (its growth direction) is altered by the oxygen ion implantation.

For steels tested at 600ºC SCW, oxygen ion implantation had no effect on the oxidation of ODS and in fact had a slight deleterious effect on the oxidation of steels NF616 and HCM12A. However, yttrium surface treatment had a pronounced beneficial effect on steels

NF616 and HCM12A for the 600ºC. HCM12A steel exhibited about 40% and NF616 steel exhibited about 25% less weight gain after exposure to SCW at 600ºC for 6 weeks, compared to their respective untreated counterparts. Yttrium surface treatment also influenced the oxidation characteristics of these two steels in two practically beneficial ways, (i) the growth kinetics of the oxide was lowered by the incorporation of yttrium in the growing oxide layer and (ii) the oxide layer is rendered markedly more dense which is desirable from the standpoints of the long term mechanical stability of the oxide, in addition to making it more impervious to ion transport.

Figure 5.5A shows a SEM cross-sectional image of the oxide layer that developed on HCM12A after exposure to SCW at 600ºC for 2 weeks and EDS compositional analysis taken at the band in the center of the oxide layer. The EDS analysis validates the presence of yttrium in oxide layer indicating that the original yttrium film oxidized and got incorporated in the growing oxide of the steel. Figure 5.5B summarizes the key results of this study and shows that hierarchy in the performance rating of the steels can be altered by surface modification.

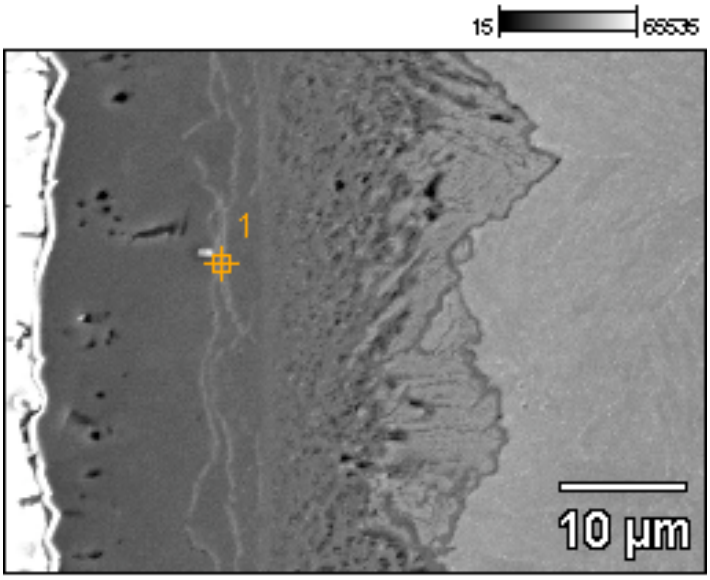

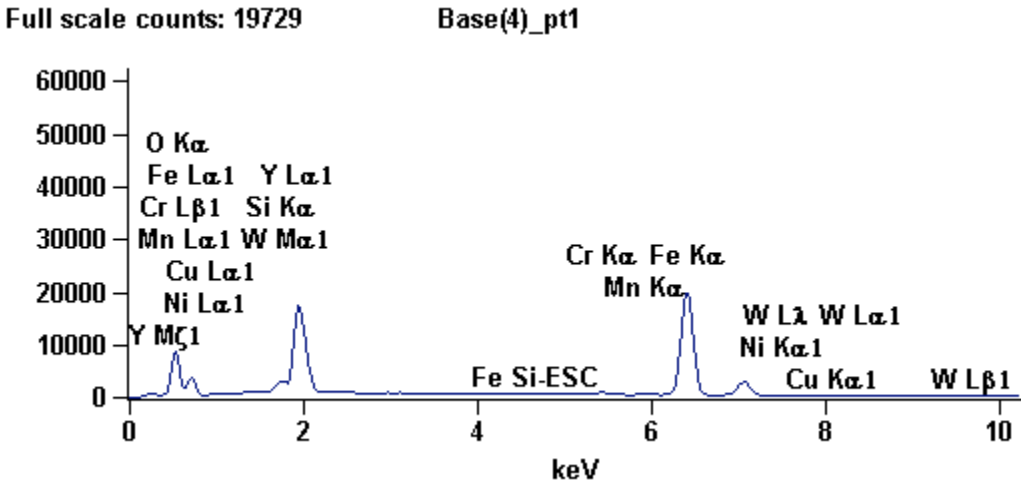

Figure 5.5A. SEM image of the oxide formed on yttrium surface treated steel HCM12A after exposure to SCW at 600ºC for 2 weeks and the EDS compositional spectrum (at region marked 1in the photograph) validating the presence of yttrium in the oxide layer.

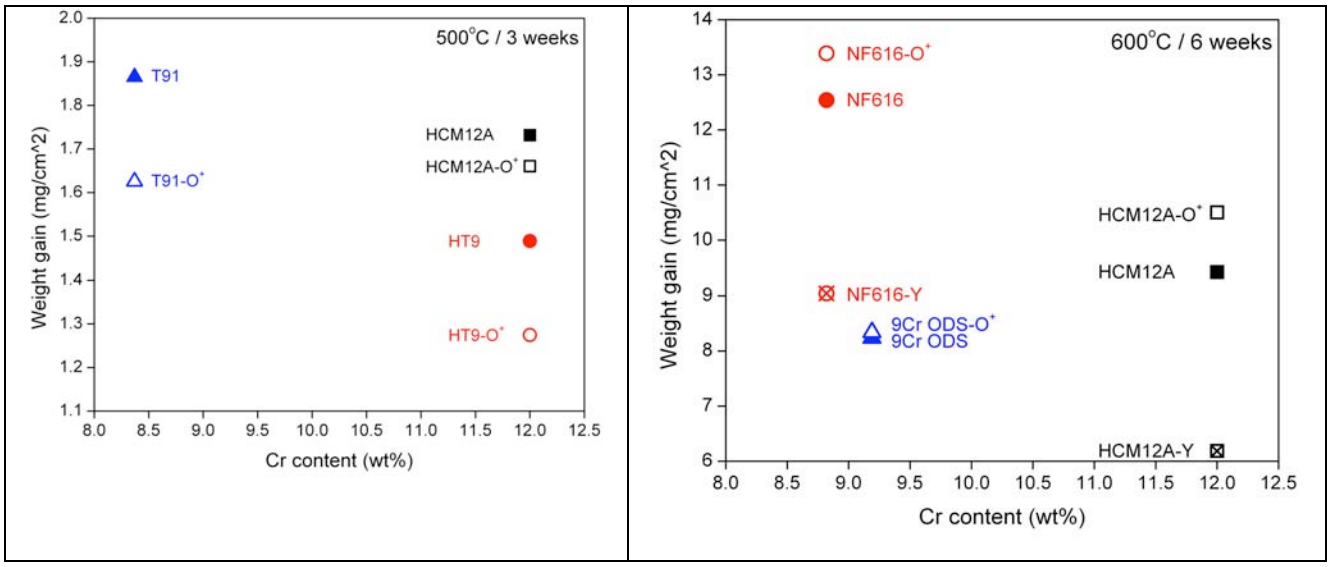

Figure 5.5B. Performance of various steels and surface treatments in SCW at 500ºC and 600ºC (25 ppb oxygen). Note that performance rating of the steels can be altered by surface modification.

5.6 Effect of Grain Boundary Engineering

Grain boundary engineering (GBE), proposed in the early 1980s is performed by a controlled sequence of thermo-mechanical processing steps (rolling and annealing) with the goal of achieving a high volume fraction of coincidence site lattice (CSL) boundaries (CSLB) in a material. The objective of GBE is to achieve a high volume fraction of low energy CSLBs, and this approach has been investigated previously with the goal of improving in creep, strength, and intergranular and stress corrosion cracking in materials.

In our studies, the as received 800H austenitic steel samples (with a prior heat treatment consisting of annealing at 1177°C for 1 hour per inch of thickness plus an additional 2 hours, followed by water quenching) were cut to sheets of thickness of 1mm and subjected to cold rolling with a thickness reduction of 7% followed by annealing at 1050°C for 90 minutes and then water quenching. This processing approach has been successfully used to increase the

population of low energy CSLBs and has been described in detail in our previous work. Optical microscopy of the surface of the 800H austenitic steel after exposure to SCW at 500°C showed spallation after about 500 hours exposure, whereas for the GBE treated samples no spallation was observed even after exposure for 1000 hours (Figure 4.6A). Figure 5.6B shows the decreased spallation of oxide on austenitic alloy 800H after exposure to SCW at 600°C for 6weeks. This is believed to be attributable to the increased population of low energy CSLBs for the GBE treated samples.

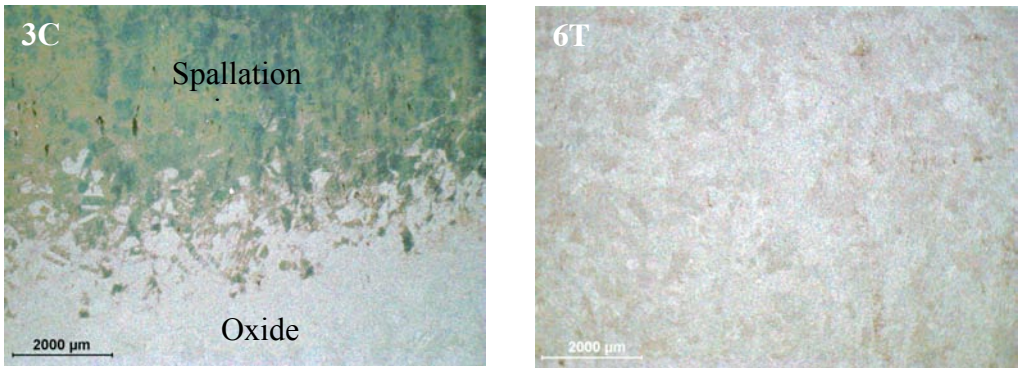

Figure 5.6A. Effect of grain boundary engineering (GBE) on oxide spallation on austenitic steel 800H after exposure to SCW at 500°C with 25 ppb oxygen content (a) as received after 500 hours exposure and (b) GBE treated after 1000 hours exposure.

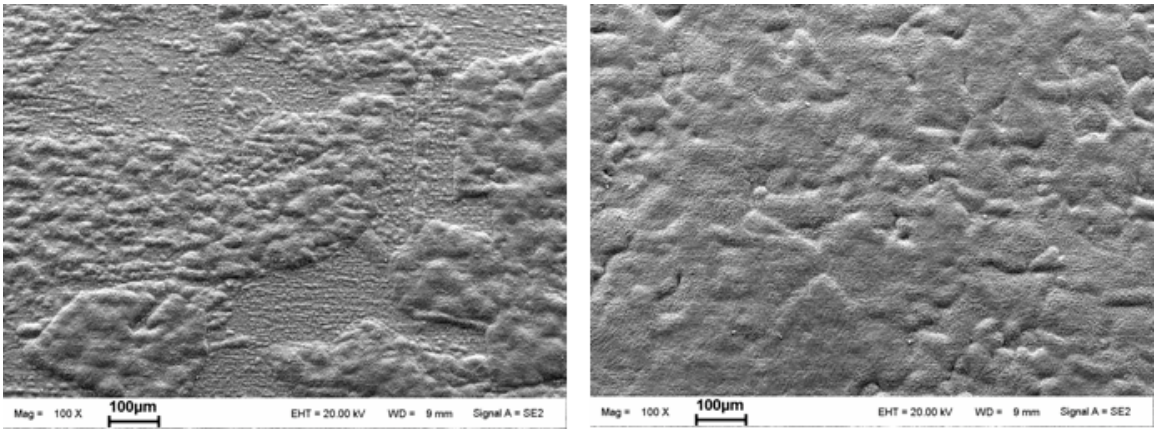

Figure 5.6B. Surface oxide formed on austenitic alloy 800H after exposure to SCW at 600°C for 6 weeks, (a) as-received 800H showing oxide spallation and (b) GBE treated 800H showing reduced spallation.

6. Conclusions and Outlook

In summary, research on the supercritical water radiation chemistry has progressed to the point that we can make reasonable order-of-magnitude estimates for radiolytic production of peroxide and hydrogen: probably around ¼ to ½ of the $G(-H_2O)$ deduced here for gamma or neutron radiolysis. A full model of the radiation chemistry in supercritical water is still a long way off. We are nearly at the point where we have the critical rate constants for pressurized water reactors in the 300-350^{o}C range, and we can estimate which reactions that are likely to be most important at higher temperature. The question, whether hydrogen water chemistry or some variant on the same theme can suppress radiolysis and stress corrosion cracking in a supercritical water cooled reactor, is not quite settled. Indications are that it can and should work to suppress radiolysis, but that higher H_2 concentration on the inlet side will be necessary.

For the near future, we will complete work on neutron radiolysis yields to investigate the effect of water density, and for both neutron and beta/gamma yields we will push the measurements to the highest temperature possible with the current apparatus. We will complete work on second order reaction rates up to 350^{o}C, and begin measurements at supercritical temperatures. With the data already in hand it should be possible to make some reasonable order-of-magnitude guesses of the corrosion potential in supercritical water, and this will be a priority of the coming year.

Scoping studies have now determined the general corrosion response of various alloy classes to supercritical water. Ferritic-martensitic steels form stable oxides with roughly parabolic kinetics and the weight gain in ferritic-martensitic steels is larger than any other alloy class and may limit their application in a SCW system. Increasing the bulk chromium concentration reduces the oxidation rate and an optimal oxygen concentration near 300 ppb may

limit the total oxide growth. Oxide dispersion strengthened steels and steels modified by adding a thin layer of yttrium significantly reduce the oxidation rate. Austenitic stainless steels show less weight gain than ferritic-martensitic steels but are more prone to spallation. The response of austenitic stainless steels as a function of alloy composition, temperature, and dissolved oxygen is complex and not as predictable as in ferritic-martensitic steels. Grain boundary engineering techniques eliminate spallation in Alloy 800H. Nickel-base alloys show very little weight gain due to oxidation, except at temperatures below the pseudo-critical point where exposure to higher density fluid increases the oxidation rate significantly. Precipitate hardened alloys are prone to pitting and part of the complex changes in weight gain seen in Ni-base alloys is a competition between pitting and general oxidation. Future studies will be aimed at defining a material and water chemistry environment that produces thin stable oxide over a range of temperatures and times. The interface with the radiolysis studies is critical to understanding corrosion in the true environment of a supercritical water reactor.

References:

1] Kent, M.C., Sims, H.E. (1992). "The yield of γ-radiolysis products from water at temperatures up to 270^{o} C" *Harwell Report AEA-RS-2303*

2] Katsumura, Y., Shiraishi, H., Hiroishi, D., Ishigure, K. (1988a). "Water radiolysis at high temperatures" *1988 Jaif Internationional Conference on Water Chemistry in Nuclear Power Plants Proceeding*. Volume 2.

3] Bartels, D.M., Takahashi, K., Cline, J.A., Marin, T.W., Jonah, C.D. (2005). "Pulse radiolysis of supercritical water. 3. Spectrum and thermodynamics of the hydrated electron" *J. Phys. Chem. A* 2005, 109, 1299-1307.

4] Laverne, J. A. *Journal of Physical Chemistry* **1988**, *92*, 2808.

5] McCracken, D.R., Tsang, K.T., Laughton, P.J. (1998). "Aspects of the physics and chemistry of water radiolysis by fast neutrons and fast electrons in nuclear reactors" AECL-11895.

6] Bonin, J.; Janik, I.; Janik, D.; Bartels, D. M. *Journal of Physical Chemistry* **in press**.

7] Janik, D/, Janik, I., Bartels, D., *Journal of Physical chemistry* **in press**

8] Olson, L., "UWNR supercritical water radiolysis experiment: Thermal-Hydraulic Analysis" UW-Madison Masters Thesis 2005

9] Edwards, E., "Determination of Pure Neutron Radiolytic Yields for use in chemical modeling of supercritical water" UW-Madison Preliminary thesis 2006

10] Pimblott, S. Private communication 2005

11] Yamaguchi, H.; Uchihori, Y.; Yasuda, N.; Takada, M.; Kitamura, H. *Journal of Radiation Research* **2005**, *46*, 333

12] Czapski, G.; Peled, E. *Israel Journal of Chemistry* **1968**, *6*, 421.